

Attribution-NonCommercial-NoDerivatives 4.0 International (CC BY-NC-ND 4.0)  
<https://creativecommons.org/licenses/by-nc-nd/4.0/>

Access to this work was provided by the University of Maryland, Baltimore County (UMBC) ScholarWorks@UMBC digital repository on the Maryland Shared Open Access (MD-SOAR) platform.

**Please provide feedback**

Please support the ScholarWorks@UMBC repository by emailing [scholarworks-group@umbc.edu](mailto:scholarworks-group@umbc.edu) and telling us what having access to this work means to you and why it's important to you. Thank you.

Received 9 January 2024, accepted 7 May 2024, date of publication 15 May 2024, date of current version 3 June 2024.

Digital Object Identifier 10.1109/ACCESS.2024.3401401

## RESEARCH ARTICLE

# Influence of the Bubbles on the Hyperspectral Reflectance and Water Color Products

CHAVAPATI GOUSE SANDHANI<sup>1</sup>, PALANISAMY SHANMUGAM<sup>1</sup>,  
SUNDARABALAN V. BALASUBRAMANIAN<sup>2,3</sup>,  
AND S. A. SANNASIRAJ<sup>1</sup>, (Senior Member, IEEE)

<sup>1</sup>Department of Ocean Engineering, Indian Institute of Technology Madras, Chennai 600036, India

<sup>2</sup>GeoSensing and Imaging Consultancy, Trivandrum 695001, India

<sup>3</sup>Goddard Earth Sciences Technology and Research II, University of Maryland at Baltimore County, Baltimore, MD 21250, USA

Corresponding author: Palanisamy Shanmugam (psanmugam@iitm.ac.in)

This work was supported in part by Indian Institute of Technology (IIT) Madras and Scholarship offered by Ministry of Human Resource Development (MHRD), and in part by the National Geospatial Programme of Department of Science and Technology of Government of India under Grant OEC1819150DSTXPSHA.

**ABSTRACT** Bubble clouds produced by wind-induced breaking surface waves are highly reflective features that significantly influence the spectral shape and magnitude of remote sensing reflectance in sea surface waters and introduce uncertainties in the water colour products derived from airborne and satellite data. Under windy conditions, the uncertainty can extend over several orders of magnitude due to the spectral enhancement effects of bubble clouds on remote sensing reflectance ( $R_{rs}$ ). In this study, the effects of bubbles on the spectral properties of  $R_{rs}$  and water colour products are investigated using radiative transfer simulations and field measurements of bubble clouds. Radiative transfer (RT) simulations with HydroLight were performed with the inputs of the inherent optical properties (IOPs) of different waters and the scattering coefficients of bubbles to generate  $R_{rs}$ , which in turn became the input for the retrieval algorithms of chlorophyll ( $Chl$ ), suspended sediments ( $SS$ ) and coloured dissolved organic matter ( $CDOM$ ), and for planning of our field experiments. The experiment data were obtained from the Chennai harbour on 15 February 2020 (from 11 am to 3 pm, local time, IST) using a set of RAMSES TriOS radiometric sensors. These measurements were made over the time period less than two minutes to capture the wave formation, breaking and dissipation conditions. HydroLight simulations and field measurement data showed that the  $R_{rs}$  spectra in the visible and near-infrared (NIR) wavelengths are significantly enhanced in the presence of bubble clouds. The effect of bubble clouds ( $b^{bub}$ ) on the water-leaving reflectance was well pronounced in clear waters than in turbid waters, particularly in the green-NIR wavelengths due to the strong backscattering of bubbles and weak backscattering of water molecules. The  $R_{rs}$  bubble cloud ratio of different water types showed more variation with the increasing effect toward the longer wavelengths. In clear ocean waters, when  $Chl \leq 1 \text{ mg m}^{-3}$ , the  $R_{rs}$  bubble cloud ratio was increased from 1.5 to 2.5 (across the visible-NIR spectrum) in the case of less bubble clouds ( $b^{bub} = 0.1 \text{ m}^{-1}$ ) and 4 to 15 in the case of more bubble clouds ( $b^{bub} > 0.9 \text{ m}^{-1}$ ). More than 50% changes were observed at higher bubble populations as confirmed by our field experiments and earlier studies. In turbid coastal waters, the effect of bubbles on the  $R_{rs}$  was less pronounced due to the strong influence of water IOPs and the weak effect of bubbles. The magnitude of the  $R_{rs}$  spectra obtained from the field experiments also increased with increasing bubble fraction/bubble density. Consequently, the error in the water colour products retrieved from the  $R_{rs}$  data was magnified due to the overestimation of  $Chl$  and  $SS$  and underestimation of  $CDOM$  in the presence of bubbles. The results presented will have significant implications for further studies on investigating the spatial effects of bubble clouds on  $R_{rs}$  data and improving the accuracy of the water colour products retrieved from satellite data.

The associate editor coordinating the review of this manuscript and approving it for publication was Yeon-Ho Chung.

**INDEX TERMS** Bubble clouds, remote sensing reflectance, radiative transfer, radiometric measurements, ocean colour, satellite data.

## I. INTRODUCTION

The water colour remote sensing instruments mounted on aircrafts or satellites operate in the visible and near-infrared wavelengths, making observations of the water colour properties such as chlorophyll (*Chl*), suspended sediments (*SS*) and coloured dissolved organic matter (*CDOM*) in inland and oceanic waters. The wind-induced breaking waves produce bubble clouds in near-surface ocean waters, which are highly reflective features and alter/enhance the spectral shape and magnitude of water-leaving radiance recorded by the remote sensing instruments. The effect of bubble clouds on the water-leaving radiance or remote sensing reflectance ( $R_{rs}$ ) is significant in the visible wavelengths and better pronounced in the longer wavelengths, which can introduce the uncertainty of several orders of magnitude in the water colour products derived from satellite data. The density, size distribution, spatial pattern, and production/penetration depth of bubbles at higher wind speeds are the factors increasingly impacting the spectral properties of water-leaving radiance.

According to the previous studies, oceanic bubbles are generated prolifically through the breaking of waves in the upper layer of ocean surface [1], [2], [3], [4], [5], [6]. The size and number density of the bubble clouds observed in oceanic waters are generally within the range of 10 – 150  $\mu\text{m}$  [7], [8] and in the order of  $10^5$  to  $10^7$   $\text{m}^3$  [9]. Larger bubbles are commonly distributed within the surface layer, while the sizes and concentrations of bubbles decrease rapidly with depth [2], [10], [11]. These bubbles undergo energy dissipation due to the physical process [6], [12], [13], [14], wave dynamics and surface currents [5] with depth. The smaller bubbles penetrate deeper into the water column at higher wind speeds and make a significant contribution to the total bubble density [15]. The bubble clouds play an important role in exchanging the gases between the ocean surface layer and atmosphere [2], [4]. Bubble clouds form whitecaps in the near-surface ocean layer, exerting a pronounced influence on the inherent optical properties as well as on the magnitude and shape of water-leaving radiance spectra and affect the distribution and intensity of underwater light fields [3], [14], [16], [17], [18].

Earlier studies have reported that the size and density of the bubble clouds entrained in the ocean surface layer change the optical properties of seawater. The influence of bubble clouds (with and without coated films) on the light scattering was previously studied using Mie theory and in-situ measurement data [9]. For example, the backscattering coefficients of bubbles increase with increasing bubble density (size and number density) [3], [9]. The bubble contribution is small in the total scattering coefficient, but it makes a significant contribution in the backscattering coefficient of seawater [3], [17], [18]. It should be noted that the backscattered signal emerging from the near-surface ocean water determines the water-leaving radiance recorded by the remote sensors, which

is the main input for various bio-optical algorithms and inversion techniques to estimate the water constituents' concentrations and optical properties. The presence of bubble clouds alters the colour of the water, causing it to appear greener compared to adjacent waters that lack bubbles [3].

Since the bubble clouds change the shape and magnitude of water-leaving radiance spectra, there is significant uncertainty in the water colour products derived from airborne or satellite data [17], [19], [20]. The higher bubble density increases the backscattering coefficient of bubbles and hence influences the remote sensing reflectance spectra of clear oceanic waters. The HydroLight simulations demonstrated a twofold increase in the spectral remote sensing reflectance in near-surface water, attributed to the presence of bubbles [3]. In clear oceanic waters ( $Chl < 1 \text{ mg m}^{-3}$ ), the bubble clouds introduce a large error in the *Chl* products [10]. However, the bubble clouds have a less effect in productive and turbid waters due to the strong backscattering of particles and weak bubble dynamics [10], [21]. The bubble clouds also change the underwater light fields and affect the underwater visibility. Thus, it is critical to study the impact of bubble clouds on the remote sensing reflectance using experiments and radiative transfer simulations. Such studies will be useful for many applications including ocean environment monitoring and assessment using the remote sensing instruments [22], [23], underwater communication [24], [25], [26], [27], [28], optical bathymetry and target detection [7], [10].

To enhance the accuracy of remotely derived water colour products, the present study investigates the impacts of bubble clouds on the remote sensing reflectance using radiative transfer simulations and field experiments. The radiative transfer simulations are performed using the inherent optical properties (IOPs) of seawater and bubbles. The in-situ experiments were conducted at a coastal site near the Chennai harbour in Bay of Bengal using a set of RAMSES TriOS radiometers. Finally, this study also investigates the uncertainty in the water colour products derived from remote sensing reflectance data.

## II. MATERIALS AND METHODS

### A. IN-SITU EXPERIMENTAL DATA

The above-water radiometric measurements were made from a set of the RAMSES TriOS hyperspectral (ARC and ACC) radiance and irradiance sensors. Three sensors were used to measure the total upwelling radiance or total water-leaving radiance ( $L_t$ ), downwelling irradiance ( $E_d$ ) and sky radiance ( $L_{sky}$ ). The remote sensing reflectance is an apparent optical property (AOP) derived from the ratio of the upwelling water-leaving radiance ( $L_w$ ) to the downwelling irradiance (i.e.,  $R_{rs}(\lambda) = L_w(\lambda) / E_d(\lambda)$ ). The water-leaving radiance ( $L_w$ ) was calculated from the  $L_t$  and  $L_{sky}$  measurements ( $L_w = L_t - \rho L_{sky}$ , where  $\rho$  is the Fresnel reflectance). The Fresnel reflectance at the sea surface varies from 0.0211 to 0.0291 for

the observation angles  $0^\circ - 40^\circ$  and wind speed  $0 - 16 \text{ m s}^{-1}$  [29]. Because of the difficulties in measuring the Fresnel reflectance under varying wind and sea surface conditions, earlier studies have adopted the optimal value of 0.028 [30], [31], [32] for the observation angles between  $30^\circ - 40^\circ$ . The in-situ measurements of the above properties were performed at the Chennai harbour in Bay of Bengal from 11 am to 3 pm (local time, IST).

The experimental site is located 500 – 700 m away from the shoreline and near the Groin structure. The sky sensor was kept away from the sun to avoid the exposure of direct sunlight [30]. The field experimental site was chosen such that it avoids the sun glint, bottom reflectance and shadow of the Groin. The viewing angle of the radiance sensor was about  $35^\circ - 40^\circ$  and positioned  $135^\circ$  [30] from the sun for measuring the total upwelling radiance. The wind speed recorded was  $4 - 5 \text{ m s}^{-1}$  throughout the day. The experiments were conducted within the time span of 30 min – 1 hour. The measurement time interval for these three sensors was 1 to 2 minutes. The field radiometric measurements were made under the calm water, wave dissipation, and breaking wave-induced bubble cloud conditions.

In addition, other properties such as *Chl* concentration ( $\text{mg m}^{-3}$ ) and turbidity (NTU) were also measured with an ECO fluorescence and turbidity sensor (i.e., ECO-FLNTU sensor, WET Labs Inc.). The FLNTU sensor provided the fluorescence chlorophyll at the excitation/emission wavelengths of 470/695 nm and turbidity at 700 nm within the same volume.

### B. LABORATORY DATA

The sea water samples were collected simultaneously in Niskon 1L bottles and stored in the mobile refrigerator (at  $4^\circ\text{C}$ ), which was kept away from the sunlight exposure. These samples were transferred to the laboratory and the standard procedures were followed to determine the concentrations of chlorophyll and suspended sediments and the absorption coefficients of phytoplankton ( $a_{ph}(\lambda)$ ) and coloured dissolved organic matter ( $a_{CDOM}(\lambda)$ ).

To determine the chlorophyll concentration, the water samples were filtered through the Whatman glass microfiber filter papers (GF/F, 47 mm diameter and pore size of  $0.7 \mu\text{m}$ ). After filtration, the filter papers were preserved in 90% (v/v) acetone for extracting the chlorophyll pigments. Subsequently, the samples were analysed in a UV-Visible spectrophotometer (UV-2600) to determine the chlorophyll concentration according to Jeffrey and Humphrey [33]. The formula to determine the chlorophyll concentration ( $\text{mg m}^{-3}$ ) is as follows [32],

$$\text{Chl} = [(11.85 \times OD_{664}) - (1.54 \times OD_{647}) - (0.08 \times OD_{630})] \times (v/V) \times 1000 \quad (1)$$

where *OD* is the optical density or absorbance, *v* is the volume of acetone (ml), and *V* is the volume of water filtered (ml).

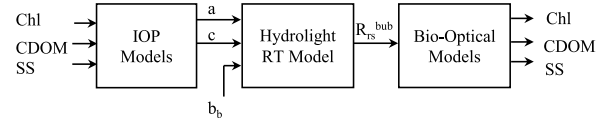


**FIGURE 1.** Schematic representation of the methodology of this study to simulate the remote sensing reflectance ( $R_{rs}$ ) spectra with the effects of bubbles and sea water constituents.

For the measurements of suspended sediments concentration, the Whatman glass microfiber filter papers (GF/F, 47 mm diameter and pore size of  $0.7 \mu\text{m}$ ) were soaked in the filtered seawater (filtered through  $0.7 \mu\text{m}$  and  $0.45 \mu\text{m}$ ) for 5 minutes. The immersed filter papers were allowed to dry in a hot air oven at  $70^\circ\text{C}$  overnight and their weight ( $w_1$ ) was measured subsequently. A similar procedure was followed to determine the final weight of the filter paper with sediment sample ( $w_2$ ). The *SS* concentration ( $\text{g m}^{-3}$ ) was determined as follows:  $SS = [(w_2 - w_1)/(V \times 0.001)]$  (where  $w_2$  and  $w_1$  are the final and initial weights of the filter papers and *V* is the volume of filtered water sample (ml)).

To determine the absorption coefficients of particulate matter ( $a_p(\lambda)$ ), another sets of water samples were collected and filtered through the Whatman glass microfiber filter papers (GF/F, 25 mm diameter and pore size  $0.7 \mu\text{m}$ ). After filtration, the filter papers were analysed in a UV-Visible spectrophotometer (UV-2600) to determine the  $a_p(\lambda)$ . After these measurements, the filter papers were placed in petri dishes, 5 – 10 ml methanol were added to these filter papers, and these samples were kept for 4 – 24 hours for extracting the phytoplankton pigments. After successfully removing the pigments, the filter papers were analysed in a UV-Visible spectrophotometer (UV-2600) to determine the absorption coefficients of detritus  $a_d(\lambda)$ . For determining the absorption coefficients of phytoplankton ( $a_{ph}(\lambda)$ ), the absorption coefficients of detritus were subtracted from the absorption coefficients of particulate matter ( $a_{ph}(\lambda) = a_p(\lambda) - a_d(\lambda)$ ).

To determine the  $a_{CDOM}(\lambda)$ , the water samples were filtered through the Whatman glass microfiber filter papers (GF/F, 47 mm and 25 mm diameter and pore size  $0.7 \mu\text{m}$ ). These water samples were again filtered through the White membrane filter papers (25 mm diameter, pore size  $0.45 \mu\text{m}$ ) and stored in *CDOM* bottles for further spectrophotometric analysis. After filtration, the filtered water samples were analysed in a UV-Visible spectrophotometer (UV-2600) to determine the  $a_{CDOM}(\lambda)$  [34], [35].

### III. METHODOLOGY

The methodology of this study on the effect of bubble clouds on the remote sensing reflectance and remotely-derived water colour products using radiative transfer simulations and field experiments is shown in Fig. 1. Accordingly, this section consists the following steps: i) IOP models, ii) Radiative transfer (RT) model, and iii) Bio-optical model. The IOP models use the sea water constituents (such as *Chl*, *SS*, and *CDOM*) as the inputs to estimate the absorption and scattering coefficients of

particulates and dissolved substances. The scattering coefficients with the bubble contribution were given as the inputs to the RT HydroLight numerical model to simulate the  $R_{rs}$  spectra. The bio-optical models were used to estimate the sea water constituents ( $Chl$ ,  $SS$ , and  $CDOM$ ) from the simulated  $R_{rs}$  data.

### A. IOP MODELS

The absorption and scattering coefficients of the sea water constituents were estimated using the IOP models. The total absorption coefficient ( $a_t(\lambda)$ ) is the sum of the absorption coefficients by pure water ( $a_w(\lambda)$ ), phytoplankton ( $a_{ph}(\lambda)$ ), coloured dissolved organic matter ( $a_{CDOM}(\lambda)$ ) and suspended sediments ( $a_{ss}(\lambda)$ ) according to

$$a_t(\lambda) = a_w(\lambda) + a_{ph}(\lambda) + a_{CDOM}(\lambda) + a_{ss}(\lambda) \quad (2)$$

where  $\lambda$  is the wavelength ranging from 400–750 nm,  $a_w(\lambda)$  is the pure water absorption coefficients taken from Pope and Fry [36]. The absorption coefficients of phytoplankton  $a_{ph}(\lambda)$  (Eq. 3) were calculated as a function of the  $Chl$  concentration [37],

$$a_{ph}(\lambda) = A(\lambda) \times 0.1072 \times [Chl]^{0.7627} \quad (3)$$

where  $A(\lambda)$  represents the specific absorption coefficients (constants) over the wavelengths from 400 to 750 nm [37]. The absorption spectra of phytoplankton follow the power-law function at 430 nm. The phytoplankton absorption spectra vary with wavelength and exhibit two prominent peaks at 443 nm and 670 nm and a weak signal in the green and near-infrared (NIR) region [38], [39], [40], [41]. The absorption coefficients of  $CDOM$  (Eq. 4) were determined based on the spectral slope factor ( $S_{CDOM} = 0.015$ ) at the reference wavelength ( $\lambda_0$ ) 430 nm. The  $CDOM$  absorption spectral curve exponentially decreases with wavelength [42], [43].

$$a_{CDOM}(\lambda) = 0.0293 \times [Chl]^{0.298} \times e^{-(S_{CDOM} \times (\lambda - \lambda_0))} \quad (4)$$

Similarly, the absorption coefficients of suspended sediments  $a_{ss}(\lambda)$  (Eq. 5) exponentially decrease with the spectral slope ( $S_{ss}$ ) of 0.009 to 0.014 in open oceanic waters [38]. The  $a_{ss}(\lambda)$  is expressed as

$$a_{ss}(\lambda) = 0.0435 \times [C_{ss}]^{1.1131} \times e^{-(S_{ss} \times (\lambda - \lambda_0))} \quad (5)$$

where  $S_{ss}$  is considered as 0.011 [38]. The non-algal particles exhibit weak absorption in the red wavelengths and strong absorption in the blue wavelengths. The concentration of suspended sediments ( $C_{ss}$ ) were also derived from the measurements of turbidity.

Another IOP parameter used in this study is the total scattering coefficient ( $b_t(\lambda)$ ) which is generally expressed as the sum of scattering due to pure water ( $b_w(\lambda)$ ), particulate matter ( $b_p(\lambda)$ ) and bubbles ( $b^{bub}(z, t, \lambda)$ ),

$$b_t(\lambda) = b_w(\lambda) + b_p(\lambda) + b^{bub}(z, t, \lambda) \quad (6)$$

where the pure water scattering coefficients  $b_w(\lambda)$  were taken from Smith and Baker [44]. The recent studies has developed a theoretical models to estimate the volume scattering function (VSF), and  $b_w(\lambda)$  for pure water [45], [46], [47], [48], [49]. The estimated  $b_w(\lambda)$  of the recent studies was compared with  $b_w(\lambda)$  were taken from Smith and Baker [44] and both studies are almost similar and shows a minimal difference. Figure 2 depicts the comparison of the remote sensing reflectance spectra simulated with HydroLight using the recently modelled scattering coefficient of pure water [46] and the scattering coefficient of pure water employed in the present study [44] for varying  $Chl$  concentration ranging from 0.05–5 mg m<sup>-3</sup>. The simulated  $R_{rs}$  results from HydroLight exhibit similarity for both the recently modelled [46] scattering coefficient of pure water and the one utilized in the present study [44] across  $Chl$  concentrations ranging from 0.05 to 5 mg m<sup>-3</sup> (Fig. 2(a)–(d)). Therefore, incorporating scattering coefficients from Smith and Baker (1981) did not induce notable changes in the outcomes when compared to the recent modelled scattering coefficients of pure water [45], [46], [47], [48], [49]. The  $b_p(\lambda)$  is the scattering coefficient of particulate matter, which includes the contribution of phytoplankton and suspended sediments particles. The  $CDOM$  was assumed to be non-scattering. The  $b_p(\lambda)$  coefficients [50] were determined from the  $Chl$  concentration with a constant factor of 0.3 [51], [52]

$$b_p(\lambda) = 0.3 \times [Chl]^{0.62} \times \left(\frac{550}{\lambda}\right) \quad (7)$$

The term  $b^{bub}(z, t, \lambda)$  (in Eq. 6) is the bubble scattering coefficient and time-dependent. Bubbles in the oceans exhibit varying concentrations and sizes, depending on wind speed. In this study, the  $b^{bub}$  coefficients were assumed to be constants (in the range of 0.1, 0.5, and 1 m<sup>-1</sup>) and stable with depth, time and wavelength.

The total backscattering coefficient ( $b_b(\lambda)$ ) is the sum of the contributions due to pure water ( $b_{bw}(\lambda)$ ), particulate matter ( $b_{bp}(\lambda)$ ) and bubbles ( $b_b^{bub}(z, t, \lambda)$ ) as defined by

$$b_b(\lambda) = b_{bw}(\lambda) + b_{bp}(\lambda) + b_b^{bub}(z, t, \lambda) \quad (8)$$

The  $b_{bw}(\lambda)$  is half of the pure water scattering coefficient [10], [44], [46]. The  $b_{bp}(\lambda)$  values were determined by dividing the particulate scattering coefficients with a coefficient of 0.018 [53]. The bubble backscattering coefficient were also considered as constants with depth and wavelength, similar to the scattering coefficient of the bubble.

In general, oceanic bubbles were generated by the wind-induced wave-breaking conditions and follow the power-law distribution. According to the previous studies [3], [7], [9], the bubble population's minimum and maximum radii and distribution slope are typically within the ranges of 5–20  $\mu$ m, 100–1000  $\mu$ m and 3.6–4.6, respectively. Using the Mie scattering theory, the backscatter fraction for 200 different bubble populations is calculated.

In particular, a fixed bubble population is chosen with a minimum size of 10  $\mu$ m, a maximum size of 200  $\mu$ m



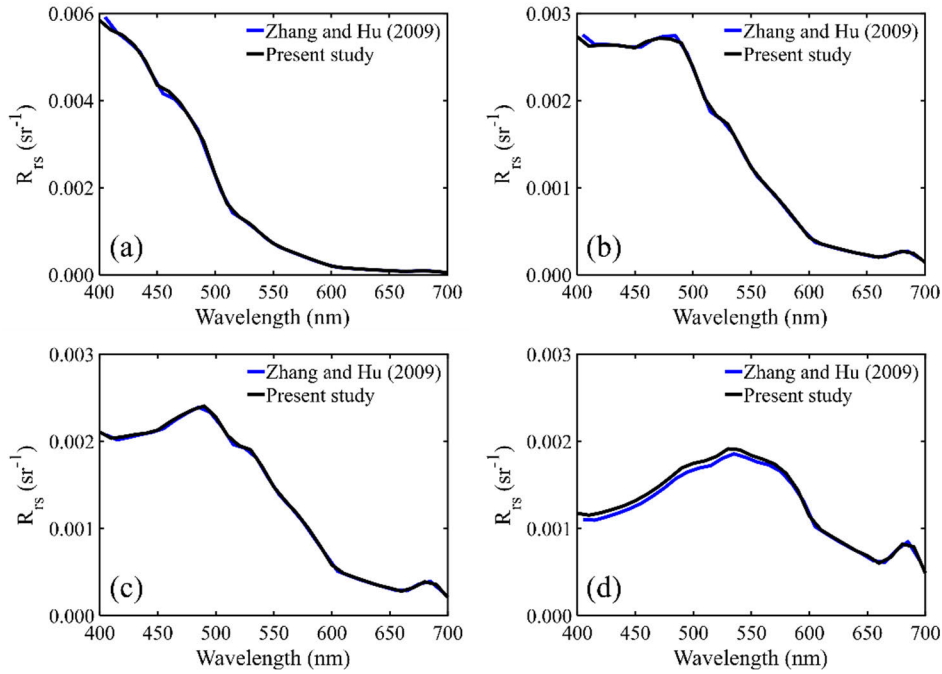


**FIGURE 2.** Comparison of the remote sensing reflectance ( $R_{rs}$ ) spectra simulated with HydroLight using the recently modelled scattering coefficient of pure water [54] and the scattering coefficient of pure water employed in the present study [44] for varying *Chl* concentrations (0.05 to 5  $\text{mg m}^{-3}$ ). (a) 0.05  $\text{mg m}^{-3}$ , (b) 0.5  $\text{mg m}^{-3}$ , (c) 1  $\text{mg m}^{-3}$ , (d) 5  $\text{mg m}^{-3}$ .

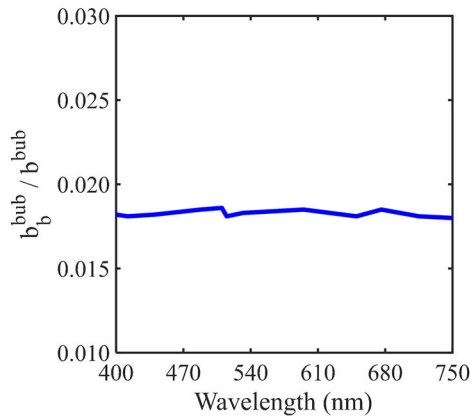


**FIGURE 3.** Backscatter fractions ( $b_b^{bub}(\lambda) / b_b^{bub}(\lambda)$ ) for a fixed bubble population at different wavelengths obtained from the Mie theory calculations.

and a slope of 4. The resulting backscatter fraction ( $b_b^{bub}(\lambda) / b_b^{bub}(\lambda)$ ) calculated (using Mie theory) for all visible wavelengths is shown in Fig. 3. The calculations indicate that the backscatter fraction for all cases is approximately 0.018. Using the concentrations of *Chl* and *SS*, the IOPs such as absorption, scattering and backscattering coefficients were calculated and used in the RT model as the inputs.

### B. RADIATIVE TRANSFER SIMULATION

This section describes the radiative transfer simulation of radiance distributions and the related quantities within and

leaving any plane-parallel water body in the presence of bubbles. For this simulation, the invariant imbedding numerical model in HydroLight (version-5.0) was utilised as it is a time-independent and one-dimensional radiative transfer model [30], [55], [56]. The HydroLight RT model generates the radiance and reflectance quantities for the infinite or finite depth of a water body. For a finite depth of water body, the model computes the Bidirectional Reflectance Distribution Function (BRDF) from the specified irradiance reflectance of the bottom boundary and the bottom is considered as the Lambertian surface. For an infinitely deep water, the model computes the BRDF up to a maximum depth ( $z_{max}$ ) and beyond this depth the inelastic scattering and internal source do not have any effect on the radiance computation. After calculating the  $z_{max}$ , the model assumes that the water column is vertically homogenous and the IOPs are constant or not changing spatially [30]. The HydroLight incorporates the Cox and Munk model [57] and MODTRAN [58] for generating the sea surface roughness from wind speeds and sky radiances, which provide the boundary conditions for the RT model. Finally, the remote sensing reflectance were determined based on the radiance distribution data.

To consider the bubbles in the radiative transfer simulation, the scattering and backscattering coefficients were incremented based on the bubble scattering coefficients from the previous studies [3], [7]. The bubble scattering coefficients ( $b_b^{bub}$ ) were considered from 0.1-1  $\text{m}^{-1}$  with the interval of 0.1  $\text{m}^{-1}$  [3]. Adding the bubble scattering coefficient and those of the water and particulate matter gives the total

scattering coefficient ( $b_t = b_t + b^{bub}$ ). Earlier studies have confirmed that the oceanic bubbles enhance the phase function at a scattering angle of  $50^\circ - 80^\circ$  [7], [18], [21]. At the critical scattering angle ( $82^\circ$ ), the phase function increases over an order due to the bubble population. The magnitude and shape of the phase function due to the higher bubble populations are different than the phase functions due to the lower bubble populations [18].

Another important parameter for solving the RT is the volume scattering function (VSF)  $\beta(\theta, \lambda)$  ( $\text{m}^{-1} \text{sr}^{-1}$ ) which defines the angular distribution of the scattered light [7], [18]. The  $\beta(\theta, \lambda)$  is expressed with the scattering coefficient ( $b$ ) as follows,

$$b = 2\pi \int_0^\pi \beta(\theta, \lambda) \sin\theta d\theta \quad (9)$$

Like the IOPs (Eqs. 2, 6, and 8),  $\beta_t(\theta, \lambda)$  can also be partitioned into the respective subcomponents as a function of the pure water, particulate matter and bubbles ( $\beta_w(\theta, \lambda)$ ,  $\beta_p(\theta, \lambda)$ , and  $\beta^{bub}(\theta, \lambda)$ , respectively)

$$\beta_t(\theta, \lambda) = \beta_w(\theta, \lambda) + \beta_p(\theta, \lambda) + \beta^{bub}(\theta, \lambda) \quad (10)$$

The VSF ( $\beta_t(z, \Psi, \lambda)$ ) can be written as the product of the scattering coefficient  $b_t(z, \lambda)$  and spectral scattering phase function  $\tilde{\beta}_t(z, \Psi, \lambda)$

$$\beta_t(z, \Psi, \lambda) = b_t(z, \lambda) \tilde{\beta}_t(z, \Psi, \lambda) \quad (11)$$

The spectral scattering phase function  $\tilde{\beta}(z, \Psi, \lambda)$  can be described over the scattering angle ( $\Psi$ ) from  $0^\circ$  to  $180^\circ$  [3]. The spectral scattering phase function can be written as  $\tilde{\beta}_t(z, \Psi, \lambda)$  ( $\text{sr}^{-1}$ )

$$\begin{aligned} \tilde{\beta}_t(z, \Psi, \lambda) = \tilde{\beta}_w(\Psi, \lambda) \frac{b_w(z, \lambda)}{b_t(z, \lambda)} + \tilde{\beta}_p(\Psi, \lambda) \frac{b_p(z, \lambda)}{b_t(z, \lambda)} \\ + \tilde{\beta}^{bub}(\Psi, \lambda) \frac{b^{bub}(z, \lambda)}{b_t(z, \lambda)} \end{aligned} \quad (12)$$

where  $\tilde{\beta}_w(\Psi, \lambda)$  is the pure water phase function [59],  $\tilde{\beta}_p(\Psi, \lambda)$  is the particle phase function and  $\tilde{\beta}^{bub}(\Psi, \lambda)$  is the bubble phase function. This study ignored the depth variation of IOPs and considered the wavelength-dependent coefficients of absorption, attenuation and phase function.

To generate the underwater light fields and remote sensing reflectance, the RT equation was solved by using the water IOPs and boundary conditions. The process of light beam passing through a medium can be explained through the RT equation as follows,

$$\begin{aligned} \cos\theta \frac{dL(z, \theta, \phi, \lambda)}{dz} = -c_t(z, \lambda) L(z, \theta, \phi, \lambda) \\ + \int_0^{2\pi} \int_0^\pi L(z, \theta', \phi', \lambda) \beta_t(z; \theta', \phi' \rightarrow \theta, \phi; \lambda) \sin\theta' d\theta' d\phi' \end{aligned} \quad (13)$$

According to the above RT equation (Eq. 13), the incident light beam passing through the water medium undergoes

losses due to the absorption and scattering processes. The combined absorption and scattering coefficients give the attenuation coefficient ( $c_t = a_t + b_t$ ). The negative sign in the RT equation is due to the loss of energy in terms of the attenuation. The direction of radiance is defined by setting the Cartesian coordinates ( $\hat{x}, \hat{y}, \hat{z}$ ).  $\theta$  is the polar angle measured in the direction of the unit vector  $\hat{z}$ , and  $\phi$  is the azimuth angle measured in the direction of the unit vector  $\hat{x}$ . The limits defined are  $0 \leq \theta \leq \pi$  and  $0 \leq \phi \leq 2\pi$ . The ocean depth is denoted as  $z$  (m), the mean sea surface as  $z = 0$ , the wavelength as  $\lambda$ , the radiance as  $L$ , and the volume scattering function as  $\beta$ . The  $\theta', \phi'$  is the change in the direction of scattering from  $\theta, \phi$ , when the light passes through a medium with length  $r$ , and the change in  $r$  is given by  $\Delta r$  ( $\theta', \phi' \rightarrow \theta, \phi$ ). When the light ( $L(r, \theta, \phi, \lambda$  where  $r$  = length of the medium,  $\Delta r$  = change in length of the medium, and angle =  $\theta$ , in units of  $\text{W m}^{-3} \text{m sr}^{-1} \text{nm}^{-1}$ ) passes through the water medium, a change in the radiance distribution is caused due to the absorption and scattering processes ( $L(r + \Delta r, \theta, \phi, \lambda)$ ).

After including the effect of bubbles, the RT equation is rewritten as

$$\begin{aligned} \cos\theta \frac{dL(z, \theta, \phi, \lambda)}{dz} = -c_t(z, \lambda) L(z, \theta, \phi, \lambda) \\ - c^{bub}(z, \lambda) L(z, \theta, \phi, \lambda) \\ + \int_0^{2\pi} \int_0^\pi L(z, \theta', \phi', \lambda) \beta_t(z; \theta', \phi' \rightarrow \theta, \phi; \lambda) \sin\theta' d\theta' d\phi' \end{aligned} \quad (14)$$

The presence of bubbles in Eq. 14 enhances the magnitude of radiance in the water column. Because the entrained bubbles in the water column can go up to a depth of several meters [3], the magnitude of the radiance will increase depending on the size, number density, and penetration depth of bubbles. Consequently, the general RT equation (Eq. 14) can be modified with the bubble terms, such as the attenuation coefficient of bubbles ( $c^{bub}$ ) (primarily due to the scattering coefficient of bubbles, as the air bubbles have little or negligible absorption) and volume scattering function of bubbles ( $\beta^{bub}$ ). Now, the RT equation is rewritten as

$$\begin{aligned} \cos\theta \frac{dL(z, \theta, \phi, \lambda)}{dz} = -c_t(z, \lambda) L(z, \theta, \phi, \lambda) \\ - c^{bub}(z, \lambda) L(z, \theta, \phi, \lambda) \\ + \int_0^{2\pi} \int_0^\pi L(z, \theta', \phi', \lambda) \beta_t(z; \theta', \phi' \rightarrow \theta, \phi; \lambda) \sin\theta' d\theta' d\phi' \\ + \int_0^{2\pi} \int_0^\pi L(z, \theta', \phi', \lambda) \beta^{bub}(z; \theta', \phi' \rightarrow \theta, \phi; \lambda) \sin\theta' d\theta' d\phi' \end{aligned} \quad (15)$$

The bubble-entrained layer changes the IOPs and radiance property in the water medium. The increase in the magnitude of  $b_t(z, \lambda)$  and VSF ( $\beta_t(z, \lambda)$ ) due to bubbles can be seen as the enhanced radiance in the visible wavelengths. The radiance simulations in the presence of bubbles can be used to

derive the water colour products and calculate the associated uncertainty.

### C. BIO-OPTICAL MODELS

The impact of bubbles on the estimation of sea water constituents (such as *Chl*, *SS*, and *CDOM*) have been investigated in numerous studies. For example, the effect of bubbles on the estimation of *Chl* concentration from remote sensing reflectance data was studied [3], [9] using a blue-green ratio algorithm [60]. It is well known that the standard blue-green ratio algorithm often produces erroneous *Chl* concentrations in turbid coastal waters as compared to the Generalized Algal Bloom Index (GABI) algorithm [32], [41]. The GABI algorithm is accurate and stable when applied to a wide range of waters within open-ocean, coastal and inland environments. Thus, our study utilised the GABI algorithm to estimate *Chl* in the presence of bubbles.

The GABI parameter  $Y_n$  was calculated as the product of the Algal bloom Index (ABI) parameter  $X$  and  $X'_n$  ( $n$  = water type). The ABI parameter  $X$  varies between 0 – 10, with a value of 0 representing the water with low chlorophyll and a value of 10 representing the water with the highest chlorophyll concentration. The parameter  $X'_1$  was derived from the normalized water-leaving radiance ( $nL_w$ ), where  $nL_w(490)$  was used due to the increased scattering and decreased absorption by the particulates and dissolved substances. The ratio of  $nL_w(670)$  and  $nL_w(680)$ , where  $nL_w(670)$  and  $nL_w(680)$  are influenced by the phytoplankton absorption-induced trough at 670 nm and fluorescence induced peak at 680 nm respectively. A combination of these parameters forms the type 1 parameter ( $X'_1$ ) for coastal and oceanic waters. The  $X'_2$  parameter was derived for moderately productive and highly turbid productive waters within coastal and inland environments. The blue-green-NIR bands were found to be accurate for moderately turbid waters and the green band was replaced with the red band for highly turbid productive waters. The non-algal particles are more dominant in moderately productive waters, where  $nL_w(555)$  works better than  $nL_w(709)$ . To calculate the parameter  $X'_2$ , the  $nL_w(443)$  band was used along with a contact factor for a better transition between the two water types. The GABI parameter ( $Y_n$ ) is expressed as,

$$Chl_{GABI} = \begin{cases} a \times Y_1^{-b} & n = 1 \\ c \times Y_2^{-d} & n = 2 \text{ (710 nm)} \\ e \times Y_2^{-f} & n = 2 \text{ (748 nm)} \end{cases} \quad (16)$$

For type 1 waters, the constant values  $a = 3.39$  and  $b = 2.992$  were derived from the power function formulation. For type 2 waters, the constant values  $c = 21.67$  and  $d = 1.31$  were used with  $nL_w(710)$ . For type 2 waters, the constant values  $e = 79.035$  and  $f = 0.909$  were used with  $nL_w(748)$ .

The suspended sediment concentration was estimated from the remote sensing reflectance through the turbidity property [37], [61]. The turbidity was estimated as the ratio of the

$R_{rs}$  values in the red-green bands, which are most affected due to high backscattering of suspended sediments. For this study, an empirical relationship proposed was used to estimate turbidity [61] and suspended sediment concentration from  $R_{rs}$  data at 555 and 670 nm. The estimated turbidity was validated using in-situ data from coastal, estuarine and harbour waters with a correlation coefficient ( $R^2$ ) of 0.88 [61]. The other turbidity algorithm [62] uses the dark spectrum fitting atmosphere correction technique, which is less applicable to many coastal and open ocean waters. The *SS* concentration was directly proportional to the turbidity [37]. The expressions are given as

$$Turbidity = 240.05 \times \left( \frac{R_{rs}(670)}{R_{rs}(670) + R_{rs}(555)} \right)^{3.0219} \quad (17)$$

$$SS = 1.3733 \times Turbidity \quad (18)$$

The absorption coefficients of *CDOM* ( $a_{CDOM}$ ) were estimated from the  $R_{rs}$  values at 443 and 555 nm [42]. Here, a simple empirical formulation was used for all water types (coastal, oceanic waters and turbid productive inland waters) which relates the  $a_{CDOM}$  to the remote sensing reflectance as follows

$$a_{CDOM}(412) = c \times \left[ \frac{R_{rs}(443)}{R_{rs}(555)} \right]^d \quad (19)$$

where  $c = 0.1866$  and  $d = -1.9668$  for all water types (Eq. 19). This formulation is generally applicable to most water types with the terrestrially-derived *CDOM* and in-situ produced *CDOM* contents [42].

### D. SENSITIVITY ANALYSIS

The impacts of bubbles on the magnitude of  $R_{rs}$  spectra were measured by using the statistical matrices such as Mean Relative Error (MRE), Root Mean Square Error (RMSE), Bias, Slope, Intercept and Correlation Coefficient ( $R^2$ ). The mean relative error was calculated between the estimated and actual values over a number of samples ( $N$ ) ( $MRE = 1/N \sum_{i=1}^{N-1} (X_{bub} - X)/X$ ). The root mean square error is the standard deviation of the predicted and actual values for all the samples ( $N$ ) ( $RMSE = \sqrt{1/N \sum_{i=1}^{N-1} (X_{bub} - X)^2}$ ). The bias is the systematic error representing the incorrect estimation of the actual values for all samples ( $N$ ) ( $1/N \sum_{i=1}^{N-1} (X_{bub} - X)$ ). The slope is the rate of change between the predicted and actual values, whereas the intercept is the value of the dependent variable when the independent variable is zero. The correlation coefficient ( $R^2$ ) determines the relationship between the predicted and actual values. Here,  $X_{bub}$  = retrieved products ( $R_{rs}$ , *Chl*, *SS* and *CDOM*) in the presence of bubbles and  $X$  = retrieved products in the absence of bubbles.

## IV. RESULTS AND DISCUSSION

### A. IMPACT OF BUBBLES ON THE REMOTE SENSING REFLECTANCE

The magnitude and shape of the remote sensing reflectance spectra change depending on the types and contents of the



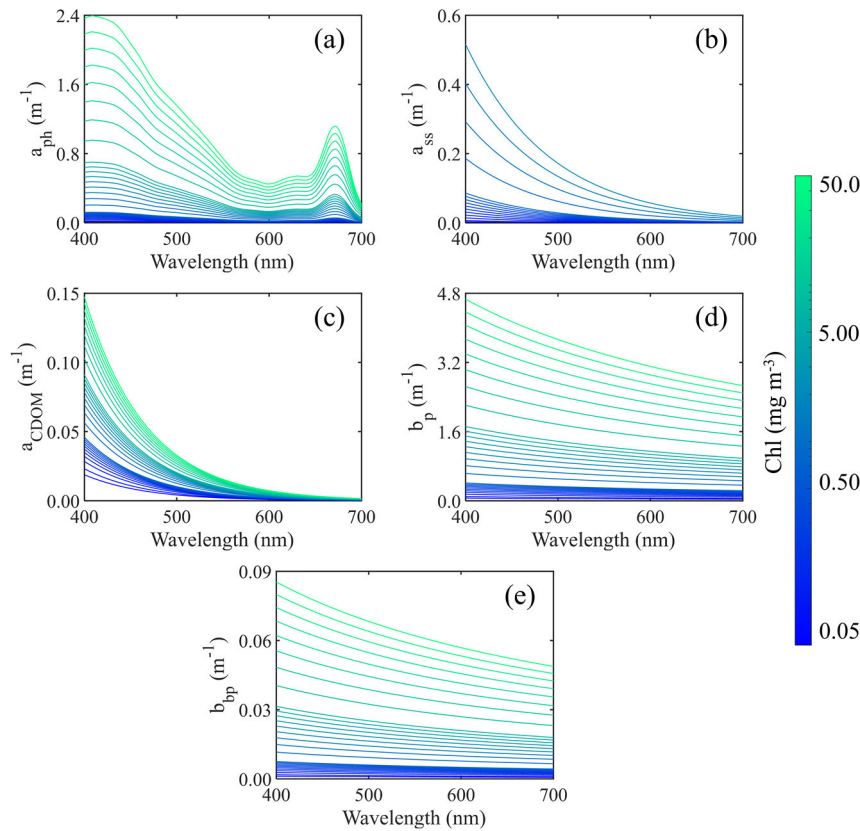


**FIGURE 4.** The modelled input parameters such as the absorption, scattering, and backscattering coefficients of sea water constituents for a range of  $Chl$  ( $0.05$  to  $50 \text{ mg m}^{-3}$ ), suspended sediments ( $0.04$  to  $6 \text{ g m}^{-3}$ ), and coloured dissolved organic matter ( $0.019$  to  $0.15 \text{ m}^{-1}$ ). The derived parameters include (a) the absorption coefficients of phytoplankton ( $a_{ph}$ ), (b) the absorption coefficients of suspended sediments ( $a_{ss}$ ), (c) the absorption coefficients of coloured dissolved organic matter ( $a_{CDOM}$ ), (d) the scattering coefficients of particulate matter ( $b_p$ ), and (e) the backscattering coefficients of particulate matter  $b_{bp}$ .

sea water constituents ( $Chl$ ,  $SS$  and  $CDOM$ ). Specifically, the magnitude of  $R_{rs}$  is affected by the breaking-wave-induced bubbles. Here, the HydroLight based invariant imbedding RT model was used to study the impacts of bubbles on the spectral shape and magnitude of  $R_{rs}$ . The water types considered in this study include type 1 waters (coastal and oceanic waters) and type 2 waters (highly productive and turbid waters). The input data (IOPs) for a wide range of sea water constituents were generated based on the expressions (described in section III-A). Figure 4 shows the spectral plots of the absorption coefficients of phytoplankton ( $a_{ph}$ ), suspended sediments ( $a_{ss}$ ) (non-algal particles) and coloured dissolved organic matter ( $a_{CDOM}$ ) as well as the scattering and backscattering coefficients of particulates in seawater.

The phytoplankton absorption coefficients (Fig. 4(a)), as calculated for a wide range of waters (with  $Chl$   $0.05$  to  $50 \text{ mg m}^{-3}$ ), exhibit peaks at the blue and red wavelengths due to the increasing  $Chl$  concentration. For example, when the  $Chl$  is  $0.05 \text{ mg m}^{-3}$ , the  $a_{ph}$  values are  $0.012 \text{ m}^{-1}$  and  $0.001 \text{ m}^{-1}$  at  $400$  and  $670 \text{ nm}$  respectively. When the  $Chl$  increases to  $0.5 \text{ mg m}^{-3}$ , the corresponding  $a_{ph}$  values rise to  $0.07 \text{ m}^{-1}$  and  $0.008 \text{ m}^{-1}$  at  $400$  and  $670 \text{ nm}$  respectively. For the  $Chl$  of  $5 \text{ mg m}^{-3}$ , the  $a_{ph}$  values are  $0.41 \text{ m}^{-1}$

at  $400 \text{ nm}$  and  $0.04 \text{ m}^{-1}$  at  $670 \text{ nm}$ . In case of the  $Chl$   $50 \text{ mg m}^{-3}$ , the  $a_{ph}$  values escalate to  $2.36 \text{ m}^{-1}$  and  $0.26 \text{ m}^{-1}$  at  $400$  and  $670 \text{ nm}$  respectively. The spectral values of  $a_{ss}$  were also calculated for a range of  $SS$  ( $0.04$  to  $6 \text{ g m}^{-3}$ ). Figure 4(b) shows the spectral plots of  $a_{ss}$ , where the values of  $a_{ss}$  reveal an increment from  $0.002 \text{ m}^{-1}$  (at  $400 \text{ nm}$ ) for  $SS$  concentration of  $0.04 \text{ g m}^{-3}$  to  $0.46 \text{ m}^{-1}$  for  $SS$  concentration of  $6 \text{ g m}^{-3}$ . Similarly, the  $a_{CDOM}$  coefficient increases with increasing  $Chl$  concentration (as shown in Fig. 4(c)). For example, the  $a_{CDOM}(400)$  values are  $0.019 \text{ m}^{-1}$ ,  $0.037 \text{ m}^{-1}$ ,  $0.074 \text{ m}^{-1}$ , and  $0.15 \text{ m}^{-1}$  for the corresponding  $Chl$  concentrations  $0.05 \text{ mg m}^{-3}$ ,  $0.5 \text{ mg m}^{-3}$ ,  $5 \text{ mg m}^{-3}$ , and  $50 \text{ mg m}^{-3}$ . The scattering coefficients of particulate matter vary with  $Chl$  concentration (as shown in Fig. 4(d)). At  $400 \text{ nm}$  the  $b_p$  values are  $0.06 \text{ m}^{-1}$ ,  $0.27 \text{ m}^{-1}$ ,  $1.12 \text{ m}^{-1}$ , and  $4.66 \text{ m}^{-1}$  for the  $Chl$  concentrations  $0.05 \text{ mg m}^{-3}$ ,  $0.5 \text{ mg m}^{-3}$ ,  $5 \text{ mg m}^{-3}$ , and  $50 \text{ mg m}^{-3}$  respectively. The backscattering coefficients of particulate matter are identical in shape of  $b_p$  despite the variation in its magnitude ( $0.001 \text{ m}^{-1}$  to  $0.08 \text{ m}^{-1}$ ) at  $400 \text{ nm}$  (Fig. 4(e)).

The invariant imbedding RT model simulated the underwater light field characteristics from the IOPs as the inputs. The outputs of this model are underwater light field parameters

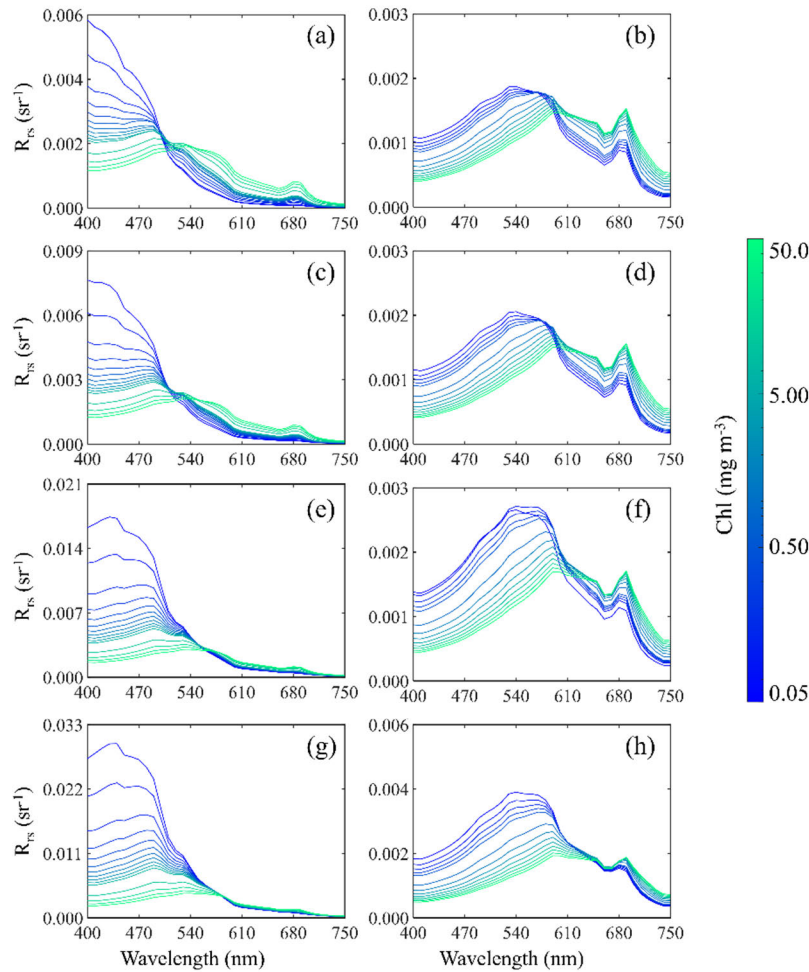


**FIGURE 5.** The effects of bubbles on the  $R_{rs}$  spectra obtained from the RT simulations for clear water (left column) and turbid water (right column) with different chlorophyll concentrations ( $0.05$  to  $50 \text{ mg m}^{-3}$ ). The  $R_{rs}$  spectra were obtained without the influence of bubbles ( $b^{bub} = 0 \text{ m}^{-1}$ ) (first row, (a)&(b)) and with the influence of bubbles ( $b^{bub} = 0.1, 0.5, 1 \text{ m}^{-1}$ ) (second, third and fourth rows, (c)-(h)).

such as radiance and irradiance and the derived AOP quantities such as the  $R_{rs}$  and diffuse attenuation coefficient. From these simulations, the  $R_{rs}$  is considered as the primary parameter for the present analysis [63], [64]. The  $R_{rs}$  spectra were generated from the IOP parameters (as shown in Fig. 4) with and without the bubbles. The scattering coefficients of bubbles ( $b^{bub} = 0.1\text{--}1 \text{ m}^{-1}$ ) for different bubble number densities were used in the RT model. The bubble number density is dependent on the wind speed and wave breaking conditions.

The influence of bubbles on the remote sensing reflectance spectra was investigated in clear oceanic waters (left column) and turbid waters (right column) with no bubbles (first row) and with bubbles (second, third and fourth rows) with the scattering coefficients of  $0.1, 0.5$  and  $1 \text{ m}^{-1}$  (Fig. 5). In the absence of bubbles, the  $R_{rs}(443)$  values were around  $0.005 \text{ sr}^{-1}$ ,  $0.003 \text{ sr}^{-1}$ ,  $0.001 \text{ sr}^{-1}$  and  $0.0005 \text{ sr}^{-1}$  for the corresponding  $Chl$  concentrations  $0.05 \text{ mg m}^{-3}$ ,  $0.5 \text{ mg m}^{-3}$ ,

$5 \text{ mg m}^{-3}$  and  $50 \text{ mg m}^{-3}$  (Fig. 5(a) & (b)). In the case of bubbles ( $b^{bub} = 0.1 \text{ m}^{-1}$ ) the  $R_{rs}(443)$  were  $0.007 \text{ sr}^{-1}$ ,  $0.003 \text{ sr}^{-1}$ ,  $0.001 \text{ sr}^{-1}$ , and  $0.0005 \text{ sr}^{-1}$  for the corresponding  $Chl$  concentrations  $0.05 \text{ mg m}^{-3}$ ,  $0.5 \text{ mg m}^{-3}$ ,  $5 \text{ mg m}^{-3}$  and  $50 \text{ mg m}^{-3}$  (Fig. 5(c) & (d)). Considering the bubble contribution with  $b^{bub} = 0.5 \text{ m}^{-1}$ , the  $R_{rs}(443)$  significantly increased to  $0.017 \text{ sr}^{-1}$  for the  $Chl$   $0.05 \text{ mg m}^{-3}$ ,  $0.006 \text{ sr}^{-1}$  for the  $Chl$   $0.5 \text{ mg m}^{-3}$ ,  $0.002 \text{ sr}^{-1}$  for the  $Chl$   $5 \text{ mg m}^{-3}$  and  $0.0005 \text{ sr}^{-1}$  for the  $Chl$   $50 \text{ mg m}^{-3}$  (Fig. 5(e) & (f)). The higher bubble contribution ( $b^{bub} = 1 \text{ m}^{-1}$ ) the magnitude of  $R_{rs}(443)$  further enhanced to  $0.03 \text{ sr}^{-1}$  for the  $Chl$   $0.05 \text{ mg m}^{-3}$ ,  $0.01 \text{ sr}^{-1}$  for the  $Chl$   $0.5 \text{ mg m}^{-3}$ ,  $0.002 \text{ sr}^{-1}$  for the  $Chl$   $5 \text{ mg m}^{-3}$  and  $0.0006 \text{ sr}^{-1}$  for the  $Chl$   $50 \text{ mg m}^{-3}$  (Fig. 5(g) & (h)).

As can be seen, the  $R_{rs}(443)$  values increased from  $0.005$  to  $0.03 \text{ sr}^{-1}$  for low  $Chl$  waters ( $0.05 \text{ mg m}^{-3}$ ) and from  $0.0005$  to  $0.0006 \text{ sr}^{-1}$  for high  $Chl$  waters ( $50 \text{ mg m}^{-3}$ ). The increment of  $R_{rs}(443)$  is in the order of six times for low

**TABLE 1.** The ratio of the remote sensing reflectance ( $R_{rs}^{(bubble)}/R_{rs}^{(no\ bubble)}$ ), bubble ratio) for the chlorophyll (*Chl*) concentrations 0.05 and 50 ( $\text{mg m}^{-3}$ ) along with the different influence of bubble contributions ( $b^{bub} = 0.1\text{--}1\text{ m}^{-1}$ ) at nine different wavelengths (nm).

Bubbles in terms of $b^{bub}$ ( $\text{m}^{-1}$ )	<i>Chl</i> ( $\text{mg m}^{-3}$ )	$R_{rs}^{(bubble)}/R_{rs}^{(no\ bubble)}$								
		412	443	488	510	532	595	650	676	715
0.1	0.05	1.34	1.44	1.51	1.53	1.57	1.76	2.01	1.86	2.25
	50	1.02	1.02	1.02	1.02	1.02	1.02	1.02	1.02	1.03
0.2	0.05	1.72	1.93	2.14	2.18	2.33	2.66	3.21	2.87	3.62
	50	1.04	1.04	1.04	1.05	1.05	1.06	1.06	1.05	1.07
0.3	0.05	2.14	2.48	2.85	2.88	3.08	3.63	4.36	3.83	5.07
	50	1.06	1.06	1.07	1.07	1.08	1.09	1.10	1.08	1.10
0.4	0.05	2.55	2.99	3.55	3.65	3.87	4.54	5.51	4.78	6.44
	50	1.08	1.08	1.10	1.10	1.11	1.12	1.13	1.11	1.14
0.5	0.05	2.96	3.52	4.25	4.40	4.69	5.48	6.66	5.74	7.81
	50	1.10	1.11	1.12	1.13	1.13	1.15	1.17	1.13	1.18
0.6	0.05	3.38	4.07	4.99	5.17	5.57	6.48	7.89	6.76	9.27
	50	1.12	1.13	1.15	1.15	1.16	1.19	1.21	1.16	1.21
0.7	0.05	3.81	4.58	5.69	5.99	6.42	7.45	9.07	7.73	10.65
	50	1.14	1.15	1.17	1.18	1.19	1.22	1.24	1.19	1.25
0.8	0.05	4.20	5.08	6.38	6.77	7.28	8.42	10.23	8.70	12.01
	50	1.16	1.17	1.19	1.21	1.22	1.25	1.27	1.21	1.29
0.9	0.05	4.59	5.57	7.06	7.55	8.18	9.45	11.48	9.72	13.39
	50	1.18	1.19	1.22	1.23	1.24	1.28	1.31	1.24	1.32
1.0	0.05	4.99	6.07	7.76	8.37	9.07	10.45	12.67	10.70	14.85
	50	1.20	1.22	1.25	1.26	1.27	1.32	1.35	1.27	1.36

*Chl* waters and one fourth only for high *Chl* waters. As the *Chl* concentration increases, the effect of bubbles on the  $R_{rs}$  spectra become minimal. The enhanced  $R_{rs}$  vary across the visible wavelengths; i.e., the magnitudes of  $R_{rs}$  at the blue wavelengths are increasingly affected in low *Chl* waters and more pronounced at the green wavelengths for moderate to higher *Chl* waters.

The change in the magnitude of  $R_{rs}$  occurred due to the corresponding change in the backscattering coefficient of bubbles. The results of this analysis based on the ratio of  $R_{rs}^{(bubble)}$  and  $R_{rs}^{(no\ bubble)}$  at nine wavelengths for different bubble contributions ( $b^{bub} = 0.1\text{--}1\text{ m}^{-1}$ ) and *Chl* concentrations 0.05 to 50  $\text{mg m}^{-3}$  are shown in Table 1. The  $R_{rs}$  bubble ratio at the visible wavelengths ranged from 1.34 to 2.25 for the lower bubble contribution ( $b^{bub} = 0.1\text{ m}^{-1}$ ). However, it increased from 2.96 to 7.81 for the moderate contribution of bubbles ( $b^{bub} = 0.5\text{ m}^{-1}$ ) and 4.99 to 14.85 for the high contribution of bubbles ( $b^{bub} = 1\text{ m}^{-1}$ ). The  $R_{rs}$  bubble ratios also varied depending on the water types. For example, the  $R_{rs}$  bubble ratio varied from 1.44 to 6.07 in clear oceanic waters (*Chl* = 0.05  $\text{mg m}^{-3}$ ) with the bubble contribution of  $b^{bub}$  (0.1 – 1  $\text{m}^{-1}$ ) at 443 nm. Only little variation in the  $R_{rs}$  bubble ratio (1.02 – 1.22) was observed for productive oceanic waters (*Chl* = 50  $\text{mg m}^{-3}$ ). The  $R_{rs}$  bubble ratio at the longer wavelengths (i.e., 715 nm) was generally more pronounced in clear oceanic waters (2.25 – 14.85) than in

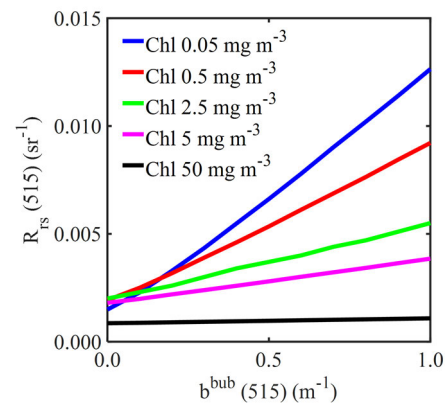


**FIGURE 6.** The impact of bubbles on the remote sensing reflectance ( $R_{rs}$ ) at 515 nm with the influence of bubbles for a wide range of *Chl* concentrations (0.05 to 50  $\text{mg m}^{-3}$ ).

turbid waters (1.03 – 1.36), due to the strong influence of the IOPs (strong scattering and weak absorption) of bubbles.

Figure 6 depicts the variation of  $R_{rs}(515)$  due to the influence of bubbles ( $b^{bub}(515)$ ) at different *Chl* concentrations. As can be seen, the bubbles tend to affect the magnitude of  $R_{rs}$  severely. At the lower *Chl* concentration (0.05  $\text{mg m}^{-3}$ ), the  $R_{rs}$  values increased with increasing  $b^{bub}$  values. The increment in the magnitude of  $R_{rs}$  caused due to the bubble contribution is 0.002 ( $b^{bub} = 0.1\text{ m}^{-1}$ ) and 0.013



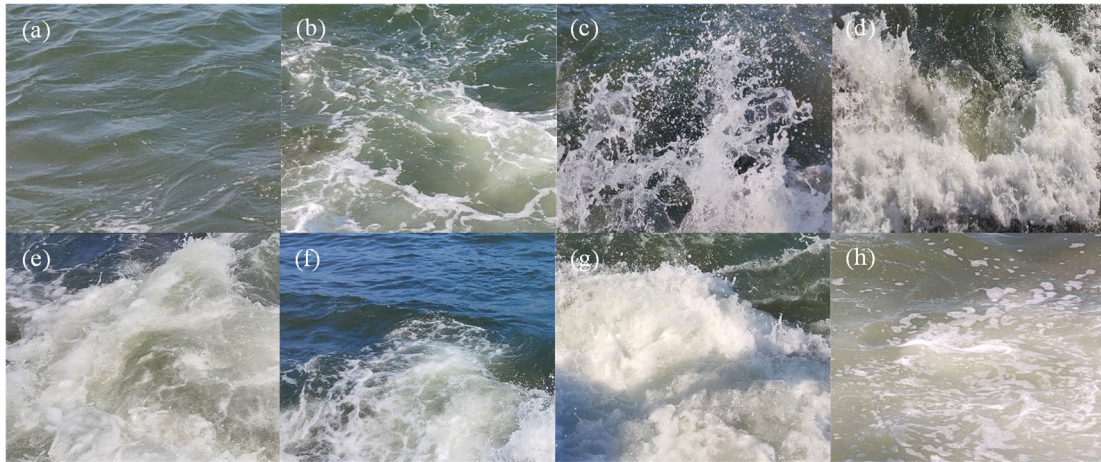


**FIGURE 7.** Photographs of the field experiments conducted at a coastal/harbour site near the Chennai port on 15 February 2020 (from 11 am to 3 pm) depicting the calm water, wave dissipation and bubble cloud formation due to the wave-breaking conditions. (a) and (b) Calm water; (c), (d) and (e) Wave dissipation and (f), (g) and (h) Bubble cloud formation due to wave breaks.

( $b^{bub} = 1 \text{ m}^{-1}$ ). It was inferred based on the influence of bubbles on the  $R_{rs}$  spectra for different  $Chl$  concentrations ( $0.05 \sim 50 \text{ mg m}^{-3}$ ) that the slope of  $R_{rs}$  spectra is markedly high ( $m=0.011$ ) for low  $Chl$  waters ( $0.05 \text{ mg m}^{-3}$ ), resulting in a large variation of  $R_{rs}$  due to the influence of bubbles. The slope of the  $R_{rs}$  spectra is very small ( $m=0.0002$ ) for high  $Chl$  waters, which indicates that the influence of bubbles is profoundly higher in clear waters than in turbid and productive waters.

## B. IMPACT OF BUBBLES ON THE REMOTE SENSING REFLECTANCE USING FIELD EXPERIMENTAL DATA

To further investigate the impact of bubbles on the  $R_{rs}$  spectra and support the simulation analysis, in-situ field experiments were conducted at a coastal site near the Chennai harbour on 15 February 2020. These experiments were conducted on a bright sunny day from 11 am to 3 pm (local time, IST) in three different water state conditions, i.e., calm water, wave-breaking-induced bubbles and wave dissipation. The water conditions were recorded using a handheld camera (Fig. 7), a set of RAMSES TriOS hyperspectral radiance and irradiance sensors and a WetLab's ECO-FLNTU sensor. The wind speeds over the day were observed around  $4 - 5 \text{ m s}^{-1}$ . The water depth at the experimental site varied from 1 m during the calm condition to 1.4 m during the wave condition. The  $Chl$  and  $SS$  concentrations varied from  $1.7 - 3.0 \text{ mg m}^{-3}$  and  $1.1 - 2.3 \text{ g m}^{-3}$  respectively. The above-water field measurements of total upwelling radiance ( $L_t$ ), downwelling irradiance ( $E_d$ ) and sky radiance ( $L_{sky}$ ) were made using a set of three RAMSES TriOS radiometers.

The sky sensor was kept away to avoid the direct sun exposure and adjacency effect. The  $L_t$  sensor was kept at a viewing angle of  $35^\circ - 40^\circ$  to measure the upwelling radiance emerging from the water with and without the presence of bubbles. The signal integration time for all the three sensors was around 1-2 minutes. The above-water in-situ field

measurements were performed such that all three conditions of no waves (calm water), wind-induced waves and wave breaks could be recorded by the radiometers. The time elapsed for calm water to calm water varied over the day with the average time interval of 1-2 min. Under these conditions, the measurements of  $L_t$ ,  $E_d$  and  $L_{sky}$  were made throughout the day from 11 am to 3 pm. The exact time (including secs) of the three water conditions was recorded for every measurement and the recorded data were segregated accordingly [65]. Finally, the  $R_{rs}$  spectra were derived from the measurements of  $L_t$ ,  $E_d$  and  $L_{sky}$  and the seawater constituents' concentrations ( $Chl$ ,  $SS$ , and  $CDOM$ ) and IOPs ( $a_{ph}$ ,  $a_{CDOM}$  and  $b_b$ ) for each measurement were determined using a laboratory spectrophotometer.

Figure 8 shows the  $a_{ph}$  and  $a_{CDOM}$  spectra along with the  $Chl$  concentrations at the study site. Specifically, the  $Chl$  concentration measured at six-time intervals of the day was  $1.7 - 3 \text{ mg m}^{-3}$ . At 11 am, the  $b_b$  varied from  $0.04 \text{ m}^{-1}$  under calm conditions with little or no bubbles to  $0.18 \text{ m}^{-1}$  under wave-breaking-induced bubbles (Fig. 8(b)). The  $R_{rs}(443)$  as  $0.008 \text{ sr}^{-1}$  and reached to  $0.02 \text{ sr}^{-1}$  due to the bubbles (Fig. 8(c)). The shift of  $b_b$  and  $R_{rs}$  was high at 11:45 am as compared to the measurements at other times. Similarly, the magnitude of  $b_b$  at  $443 \text{ nm}$  ( $0.09 \text{ m}^{-1}$ ) was enhanced reaching up to  $1.13 \text{ m}^{-1}$  for calm water conditions (Fig. 8(e)). The enhanced scattering or backscattering signal showed a profound effect on the  $R_{rs}$  spectra ( $0.009 - 0.06 \text{ sr}^{-1}$ ) (Fig. 8(f)). At the noon time (12:30 pm), the values of  $b_b(443)$  and  $R_{rs}(443)$  fluctuated in the range of  $0.13 \text{ m}^{-1}$ , and  $0.014 \text{ sr}^{-1}$  under the calm conditions and  $0.5 \text{ m}^{-1}$ , and  $0.04 \text{ sr}^{-1}$  under bubble conditions (Fig. 8(h) & (i)).

At 1:00 pm, the values of  $R_{rs}(443)$  ranged from  $0.013 \text{ sr}^{-1}$  for no bubbles and  $0.03 \text{ sr}^{-1}$  for bubble conditions (Fig. 8(l)) and the corresponding values of  $b_b(443)$  were  $0.09 \text{ m}^{-1}$  (calm) and  $0.22 \text{ m}^{-1}$  (bubbles) from the in-situ measurements (Fig. 8(k)). At 1:30 pm, the values of  $b_b$  varied



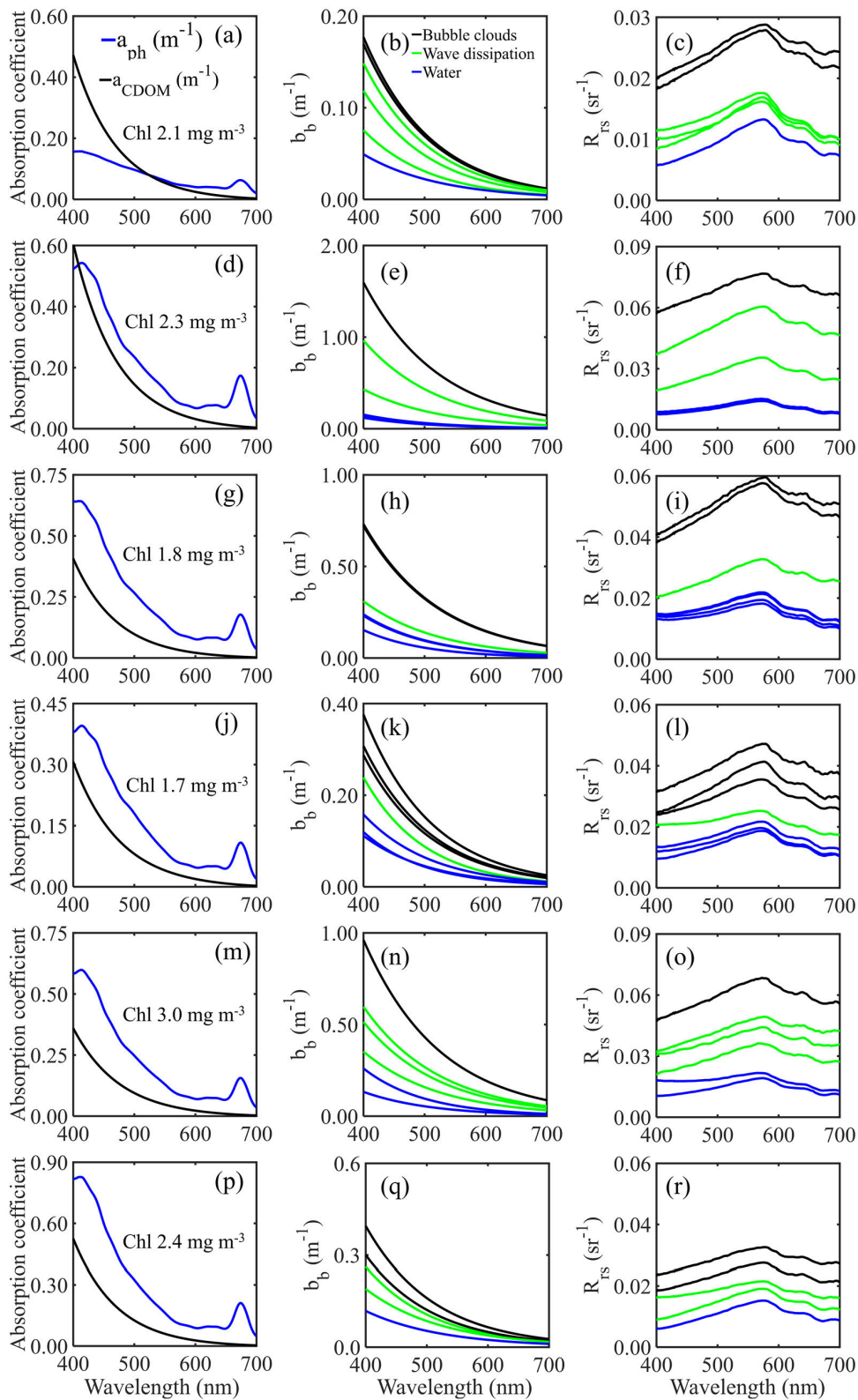


**FIGURE 8.** In-situ measurements of the absorption coefficients of phytoplankton and *CDOM* at the coastal site near the Chennai harbour 15 February 2020 (from 10 am to 3 pm). Remote sensing reflectance ( $R_{rs}$ ) spectra and backscattering coefficient ( $b_b$ ) of water (blue), wave dissipation (green), and bubble cloud formation due to the wave breaks (black). (a), (b) and (c) 11:00 am; (d), (e) and (f) 11:45 am; (g), (h) and (i) 12:30 pm; (j), (k) and (l) 1:00 pm; (m), (n) and (o) 1:30 pm; and (p), (q) and (r) 02:45 pm.

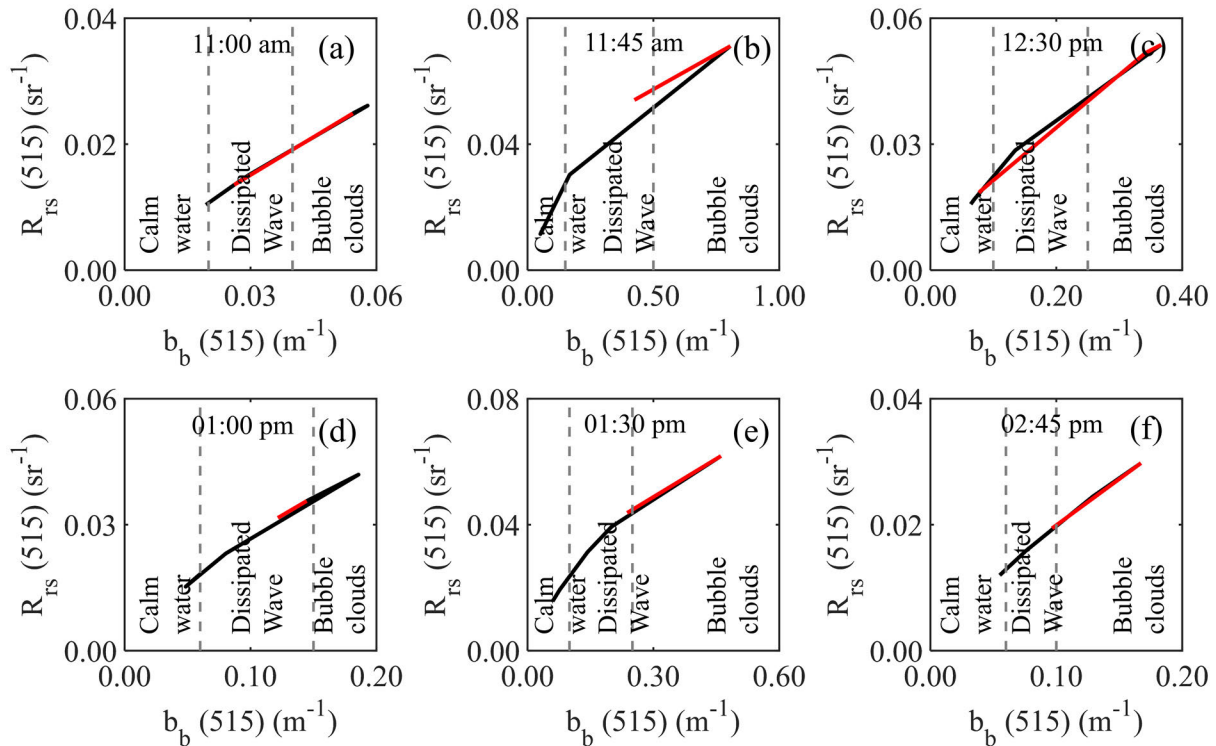


**FIGURE 9.** The remote sensing reflectance spectra and backscattering coefficient at a wavelength 515 nm for calm water, wave dissipation conditions, and wave-breaking bubbles. The black solid line represents the sequence of sea state conditions such as calm water, wave dissipation and bubble cloud generation. The red solid line represents the sea state returning to the normal (calm) after the bubble clouds dissipated in the water column.

from  $0.13 - 0.68 \text{ m}^{-1}$  (Fig. 8(n)) and a similar variation was observed in the values of  $R_{rs}$  from  $0.015$  to  $0.05 \text{ sr}^{-1}$  (Fig. 8(o)).

At 2:45 pm, the values of  $a_{ph}(443)$  were higher than those of other time periods ( $0.67 \text{ m}^{-1}$ ), whereas the values of  $a_{CDOM}(443)$  (Fig. 8(p)) and  $Chl$  were observed to be around  $0.28 \text{ m}^{-1}$  and  $2.4 \text{ mg m}^{-3}$  respectively. The values of  $b_b(443)$  were about  $0.08 \text{ m}^{-1}$  for calm ocean conditions and  $0.24 \text{ m}^{-1}$  for bubble conditions (Fig. 8(q)). The higher values observed around the noon were caused by the increased effect of bubble clouds. These results indicate that the effect of bubbles is minimum on the magnitude of  $R_{rs}$  spectra for calm water conditions and maximum for entrained bubble waters. Also note that the effect of bubbles on the spectral signature of  $R_{rs}$  increases with increasing bubble clouds.

Figure 9 shows the variation of bubble density in terms of the  $b_b$  coefficient along with the  $R_{rs}$  for calm water, wave dissipation and bubble clouds over the day. This analysis depicts the change of  $R_{rs}$  with a higher magnitude for bubbles and a lower magnitude for calm conditions (Fig. 9). The variation of bubbles can be described in terms of  $b_b(515)$ . Clearly, the magnitude of  $b_b$  increases as the bubble cloud density increases. A similar increase in the magnitude of  $R_{rs}(515)$  can be observed for calm water and wave-breaking-induced bubbles. Figure 9(a) shows the variation of  $b_b$  with respect to

the  $R_{rs}$  spectra measured at 11:00 am. The steep slope ( $0.4$ ) of  $b_b(515)$  and  $R_{rs}(515)$  indicates that the produced bubbles had taken less time to burst in the water column. The bubble number density generated at 11:00 am was decreased at other time periods (shown in Fig. 9(a)). The impact of bubbles on the  $R_{rs}$  was also verified by comparing the statistical results for calm water and bubble clouds at 11:00 am (i.e., in terms of MRE (152%) and RMSE (0.02)). A minimal impact of bubbles on the  $R_{rs}$  spectra was observed at 11:00 am, because the bubbles took less time to collapse as can be clearly seen with a steep slope ( $m=0.4$ ) in Fig. 9(a).

The life time of bubbles was higher at 11:45 am resulting in a higher impact on the  $R_{rs}$  spectra. The life time of the bubble was represented in terms of the smooth rise of  $R_{rs}$  magnitude and  $b_b$  variation with a gradual slope ( $m=0.08$ ) (Fig. 9(b)). As a result, the error was high with the  $R_{rs}$  spectra (MRE=468% and RMSE=0.06). Similarly, the impacts of bubbles on the  $b_b$  and  $R_{rs}$  spectra were studied for different time periods from 12:30 pm ( $m = 0.12$ , MRE=241% and RMSE=0.04), 1:00 pm ( $m = 0.20$ , MRE=175% and RMSE=0.02), 1:30 pm ( $m = 0.11$ , MRE=294% and RMSE=0.05) and 2:45 pm ( $m = 0.16$ , MRE=148% and RMSE=0.02) (shown in Fig. 9(c)-(f)). This analysis depicted that the deviation of  $R_{rs}$  spectra for different bubble conditions is dependent on the time of observations and bubble density.

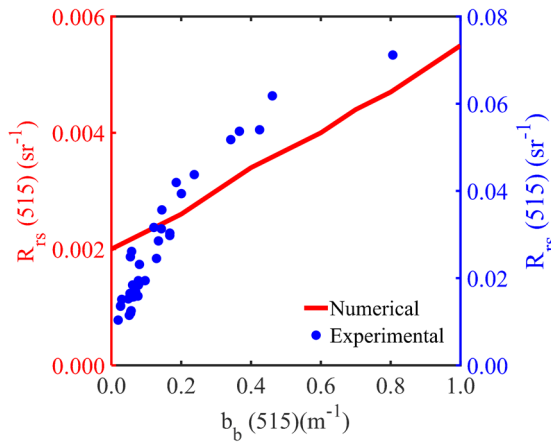


**FIGURE 10.** The simulation (red – primary y axis) and experimental (blue – secondary y axis) results of remote sensing reflectance ( $R_{rs}$ ) plotted against the bubble contributions in terms of the backscattering coefficient ( $b_b$ ) at a wavelength of 515 nm for oceanic waters with the chlorophyll concentration  $2\text{--}2.5\text{ mg m}^{-3}$ . The red line indicates the RT simulation results from the Hydrolight numerical model and the blue marker points represent the experimental results from a coastal site near the Chennai harbour.

### C. THE UNCERTAINTIES ASSOCIATED WITH THE REMOTE SENSING REFLECTANCE AND BIOGEOCHEMICAL PRODUCTS

The uncertainties associated with the  $R_{rs}$  and biogeochemical products due to the bubbles were investigated by comparing the simulated results with the experimental data. Figure 10 shows a relationship of RT model results (marked by red colour) with experimental data (marked by blue colour) (using the values of  $b_b(515)$  and  $R_{rs}(515)$ ). As demonstrated in the previous section, both simulated and experimental data showed an increase in the  $R_{rs}$  values with increasing bubble contributions (in  $b_b$  values). The statistical analysis performed between simulated and experimental  $R_{rs}$  data also showed this trend at  $Chl\ 2.5\text{ mg m}^{-3}$ . In this case,  $b^{bub} = 0.1\text{ m}^{-1}$ , MRE 0.2, RMSE 0.0003, and slope 0.003;  $b^{bub} = 0.5\text{ m}^{-1}$ , MRE 0.9, RMSE 0.0017, and slope 0.003; and  $b^{bub} = 1.0\text{ m}^{-1}$ , MRE 1.8, RMSE 0.0035, and slope 0.003. The difference in the  $R_{rs}$  spectra between experimental and simulation data is mainly caused due to the lack of parameterizations to account for the bubble contributions in the IOP models.

Consequently, we investigated the errors in the retrieved biogeochemical products ( $Chl$ ,  $SS$  and  $CDOM$ ) using the simulated  $R_{rs}$  data with bubble effects. Figure 11 shows a comparison of the seawater constituents' concentrations retrieved from the simulated  $R_{rs}$  data with and without the influence of bubbles. These water constituents were estimated using the bio-optical algorithms reported in our earlier studies [32], [37], [41], [61] (section III-C). When  $b^{bub} = 0.1\text{ m}^{-1}$ , the errors in  $Chl$  retrievals are: MRE -0.465, RMSE 13.849, Bias -7.960, Slope 0.242, Intercept 0.6907 and  $R^2\ 0.972$  (Fig. 11(a)). The errors in  $Chl$  retrievals further increased (i.e., underestimations of  $Chl$ ) with increasing

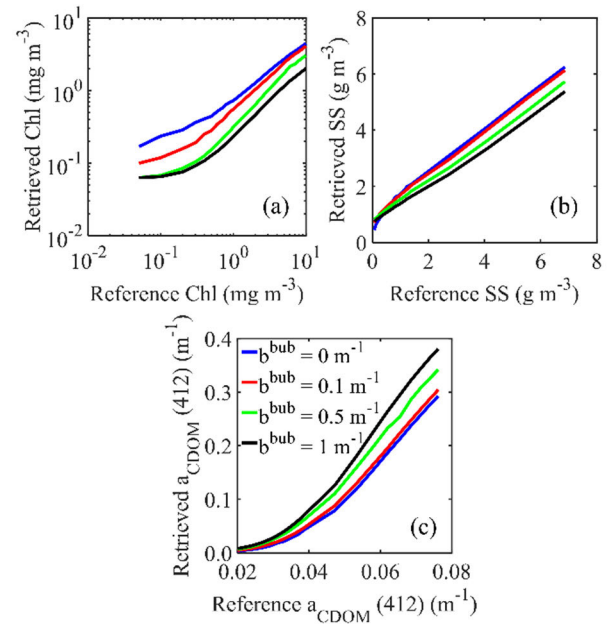


**FIGURE 11.** Comparison of the retrieved seawater constituents' concentrations from the bio-optical algorithms using the simulated  $R_{rs}$  data without the contributions of bubbles and with the contributions of bubbles. The seawater constituents are (a) Chlorophyll concentration  $Chl$ , (b) Suspended sediment concentration  $SS$ , and (c) Coloured dissolved organic matter  $a_{CDOM}(412)$ .

bubble effects ( $b^{bub} = 0.5$  and  $1.0\text{ m}^{-1}$ ). A similar trend is observed in the  $SS$  product with the influence of different bubble contributions (Fig. 11(b)); for example, when  $b^{bub} = 0.1\text{ m}^{-1}$ : MRE -0.938, RMSE 17.608, Bias -10.713, Slope 0.064, Intercept -0.031 and  $R^2\ 0.998$ . These errors are further magnified with the increasing bubble contribution as denoted by  $b^{bub} = 0.5$  and  $1.0\text{ m}^{-1}$ . In contrast, the  $a_{CDOM}$  coefficients are overestimated when compared to the reference values (Fig. 11(c)). For example, when  $b^{bub} = 0.1\text{ m}^{-1}$ : MRE 1.502, RMSE 0.205, Bias 0.142, Slope 5.435, Intercept -0.136, and  $R^2\ 0.983$ ; and when  $b^{bub} = 1\text{ m}^{-1}$ : MRE 2.302, RMSE 0.252, Bias 0.186, Slope 6.083, Intercept -0.132 and  $R^2\ 0.973$ .

The uncertainty analysis demonstrated that the oceanic bubbles have a significant impact on the simulated and experimental  $R_{rs}$  spectra. The increase in the magnitude of  $R_{rs}$  spectra due to the bubbles leads to the magnification of errors in the retrieved biogeochemical products. The results also indicate that a fraction of the error could come from the RT model as the result of the inadequate/ inaccurate parameters to account for different bubble contributions.

### V. CONCLUSION

The RT simulations and experimental data were used to demonstrate the influence of oceanic bubbles on the  $R_{rs}$  spectra and the accuracy of biogeochemical products in the presence of bubble contributions. The RT simulations were based on the measured IOPs ( $a_t$ ,  $c_t$ , and  $b_{bt}$ ) in

different oceanic waters with  $Chl$   $0.05 - 50 \text{ mg m}^{-3}$  and  $SS$   $0.04 - 6 \text{ g m}^{-3}$ . The influence of bubbles was considered through the  $b^{bub}$  coefficients in the range of  $0.1$  to  $1.0 \text{ m}^{-1}$ . For comparative analyses, simulations were performed with and without the influence of bubbles and the outputs of the simulations for clear oceanic waters varied in the range of  $R_{rs}(443) = 0.007 \text{ sr}^{-1}$ ,  $0.017 \text{ sr}^{-1}$  and  $0.03 \text{ sr}^{-1}$  for the corresponding  $b^{bub} = 0.1 \text{ m}^{-1}$ ,  $0.5 \text{ m}^{-1}$ , and  $1.0 \text{ m}^{-1}$  ( $Chl = 0.05 \text{ mg m}^{-3}$ ). In turbid oceanic waters, the values of  $R_{rs}(443)$  were  $0.0005 \text{ sr}^{-1}$ ,  $0.0005 \text{ sr}^{-1}$  and  $0.0006 \text{ sr}^{-1}$  for the corresponding  $b^{bub}$  values  $0.1 \text{ m}^{-1}$ ,  $0.5 \text{ m}^{-1}$  and  $1.0 \text{ m}^{-1}$  ( $Chl = 50 \text{ mg m}^{-3}$ ). The changes in  $R_{rs}$  spectra were also examined at other wavelengths in the visible region. The incremental increase in the magnitude of  $R_{rs}$  spectra was found to be in the order of six times in clear oceanic waters (low  $Chl$ ) and one fourth only in turbid coastal waters (with elevated  $Chl$ ). This indicates that the impact of bubbles on the  $R_{rs}$  spectra is higher in clear oceanic waters than in turbid coastal waters [3], [9], [10].

To investigate the influence of bubbles on the  $R_{rs}$  spectra, the field experiments were conducted on a bright sunny day from 11 am to 3 pm (local time, IST) at a coastal site north of the Chennai harbour. The measurements were taken sequentially to cover all three conditions – no waves (calm water), wind-generated waves, and wave-breaking and dissipation – using the RAMSES TriOS radiometers and FLNTU photometer. The experimental analysis showed that the magnitude of the  $R_{rs}$  spectra increase with the increasing contribution of bubbles (in terms of  $b_b$ ). The impact of bubbles on the magnitude of  $R_{rs}$  spectra was incremented from  $0.01 \text{ sr}^{-1}$  (calm water) to  $0.06 \text{ sr}^{-1}$  (bubble presence). This change was in the order of more than six times for clear waters than for turbid coastal waters due to high wind speeds and bubble density.

The uncertainty analysis demonstrated that the magnitude of  $R_{rs}$  is significantly increased in the presence of bubbles and resulted a large error in the retrieved biogeochemical products. This potentially limits the water colour applications and scientific analysis under high wind speeds and wave conditions. Further improvement in the bubble parameterizations (for the RT model) will produce more accurate radiometric quantities and AOP products for oceanic waters under different bubble conditions. With rapidly advanced current and future remote sensing technology in terms of spatial, spectral and radiometric resolution, the improved biogeochemical products can be obtained from this study for various water colour applications and scientific analysis.

## REFERENCES

- [1] D. M. Farmer, S. Vagle, and A. D. Booth, "A free-flooding acoustical resonator for measurement of bubble size distributions," *J. Atmos. Ocean. Technol.*, vol. 15, no. 5, pp. 1132–1146, Oct. 1998, doi: [10.1175/1520-0426\(1998\)015<1132:AFFARF>2.0.CO;2](#).
- [2] E. Lamarrea and W. K. Melville, "Sound-speed measurements near the ocean surface," *J. Acoust. Soc. Amer.*, vol. 96, no. 6, pp. 3605–3616, 1994, doi: [10.1121/1.410578](#).
- [3] D. Stramski and J. Tegowski, "Effects of intermittent entrainment of air bubbles by breaking wind waves on ocean reflectance and underwater light field," *J. Geophys. Res. Ocean.*, vol. 106, no. C12, pp. 31345–31360, 2001, doi: [10.1029/2000jc000461](#).
- [4] S. A. Thorpe, "Bubble clouds and the dynamics of the upper ocean," *Quart. J. Roy. Meteorological Soc.*, vol. 118, no. 503, pp. 1–22, 1992, doi: [10.1002/qj.49711850302](#).
- [5] S. A. Thorpe and A. J. Hall, "The characteristics of breaking waves, bubble clouds, and near-surface currents observed using side-scan sonar," *Cont. Shelf Res.*, vol. 1, no. 4, pp. 353–384, 1983, doi: [10.1016/0278-4343\(83\)90003-1](#).
- [6] H. Medwin, "In situ acoustic measurements of bubble populations in coastal ocean waters," *J. Geophys. Res.*, vol. 75, no. 3, pp. 599–611, Jan. 1970, doi: [10.1029/JC075i003p00599](#).
- [7] B. R. Angara, P. Shanmugam, and H. Ramachandran, "Inversion of volume scattering function for estimation of bubble size distribution in ocean waters," *IEEE Access*, vol. 9, pp. 135069–135078, 2021, doi: [10.1109/ACCESS.2021.3115253](#).
- [8] H. Czerski, M. Twardowski, X. Zhang, and S. Vagle, "Resolving size distributions of bubbles with radii less than  $30 \mu\text{m}$  with optical and acoustical methods," *J. Geophys. Res. Ocean.*, vol. 116, no. 11, pp. 1–13, 2011, doi: [10.1029/2011JC007177](#).
- [9] X. Zhang, M. Lewis, and B. Johnson, "Influence of bubbles on scattering of light in the ocean," *Appl. Opt.*, vol. 37, no. 27, p. 6525, 1998, doi: [10.1364/ao.37.006525](#).
- [10] L. Ma, F. Wang, C. Wang, C. Wang, and J. Tan, "Monte Carlo simulation of spectral reflectance and BRDF of the bubble layer in the upper ocean," *Opt. Exp.*, vol. 23, no. 19, p. 24274, Sep. 2015, doi: [10.1364/OE.23.024274](#).
- [11] L. Zedel and D. Farmer, "Organized structures in subsurface bubble clouds: Langmuir circulation in the open ocean," *J. Geophys. Res.*, vol. 96, no. C5, p. 8889, 1991, doi: [10.1029/91jc00189](#).
- [12] T. G. Bell, "Estimation of bubble-mediated air-sea gas exchange from concurrent DMS and  $\text{CO}_2$  transfer velocities at intermediate-high wind speeds," *Atmos. Chem. Phys.*, vol. 17, no. 14, pp. 9019–9033, 2017, doi: [10.5194/acp-17-9019-2017](#).
- [13] R. S. Bortkovskii, B. N. Egorov, V. M. Kattsov, and T. V. Pavlova, "Model estimates for the mean gas exchange between the ocean and the atmosphere under the conditions of the present-day climate and its changes expected in the 21st century," *Izv. Atmos. Ocean. Phys.*, vol. 43, no. 3, pp. 378–383, 2007, doi: [10.1134/S0001433807030127](#).
- [14] H. M. Dierssen, "Hyperspectral measurements, parameterizations, and atmospheric correction of whitecaps and foam from visible to shortwave infrared for ocean color remote sensing," *Frontiers Earth Sci.*, vol. 7, pp. 1–18, Feb. 2019, doi: [10.3389/feart.2019.00014](#).
- [15] K. Randolph, H. M. Dierssen, M. Twardowski, A. Cifuentes-Lorenzen, and C. J. Zappa, "Optical measurements of small deeply penetrating bubble populations generated by breaking waves in the Southern ocean," *J. Geophys. Res. Ocean.*, vol. 119, no. 2, pp. 757–776, Feb. 2014, doi: [10.1002/2013JC009227](#).
- [16] K. D. Moore, K. J. Voss, and H. R. Gordon, "Spectral reflectance of whitecaps: Their contribution to water-leaving radiance," *J. Geophys. Res. Ocean.*, vol. 105, no. C3, pp. 6493–6499, 2000, doi: [10.1029/1999jc900334](#).
- [17] E. J. Terrill, W. K. Melville, and D. Stramski, "Bubble entrainment by breaking waves and their influence on optical scattering in the upper ocean," *J. Geophys. Res. Ocean.*, vol. 106, no. C8, pp. 16815–16823, 2001, doi: [10.1029/2000jc000496](#).
- [18] X. Zhang, M. Lewis, M. Lee, B. Johnson, and G. Korotaev, "The volume scattering function of natural bubble populations," *Limnol. Oceanogr.*, vol. 47, no. 5, pp. 1273–1282, 2002, doi: [10.4319/lo.2002.47.5.1273](#).
- [19] B. Yan, B. Chen, and K. Stamnes, "Role of oceanic air bubbles in atmospheric correction of ocean color imagery," *Appl. Opt.*, vol. 41, no. 12, p. 2202, 2002, doi: [10.1364/ao.41.002202](#).
- [20] J. Piskozub, D. Stramski, E. Terrill, and W. K. Melville, "Small-scale effects of underwater bubble clouds on ocean reflectance: 3-D modeling results," *Opt. Exp.*, vol. 17, no. 14, p. 11747, 2009, doi: [10.1364/oe.17.011747](#).
- [21] M. Twardowski, "The optical volume scattering function in a surf zone inverted to derive sediment and bubble particle subpopulations," *J. Geophys. Res. Ocean.*, vol. 117, no. 2, pp. 1–18, 2012, doi: [10.1029/2011JC007347](#).



- [22] R. Dickie, R. Cahill, V. Fusco, H. S. Gamble, and N. Mitchell, "THz frequency selective surface filters for Earth observation remote sensing instruments," *IEEE Trans. Terahertz Sci. Technol.*, vol. 1, no. 2, pp. 450–461, Nov. 2011, doi: [10.1109/TTHZ.2011.2129470](#).
- [23] R. Müller, "Calibration and verification of remote sensing instruments and observations," *Remote Sens.*, vol. 6, no. 6, pp. 5692–5695, 2014, doi: [10.3390/rs6065692](#).
- [24] S. K. Sahu and P. Shanmugam, "A study on the effect of scattering properties of marine particles on underwater optical wireless communication channel characteristics," in *Proc. Ocean. Aberdeen*, Oct. 2017, pp. 1–7, doi: [10.1109/OCEANSE.2017.8084720](#).
- [25] S. K. Sahu and P. Shanmugam, "A theoretical study on the impact of particle scattering on the channel characteristics of underwater optical communication system," *Opt. Commun.*, vol. 408, pp. 3–14, Jun. 2017, doi: [10.1016/j.optcom.2017.06.030](#).
- [26] R. Sahoo, S. K. Sahu, and P. Shanmugam, "Estimation of the channel characteristics of a vertically downward optical wireless communication link in realistic oceanic waters," *Opt. Laser Technol.*, vol. 116, pp. 144–154, Feb. 2019, doi: [10.1016/j.optlastec.2019.03.023](#).
- [27] R. Sahoo and P. Shanmugam, "Effect of the complex air-sea interface on a hybrid atmosphere-underwater optical wireless communications system," *Opt. Commun.*, vol. 510, Jan. 2022, Art. no. 127941, doi: [10.1016/j.optcom.2022.127941](#).
- [28] B. R. Angara, P. Shanmugam, and H. Ramachandran, "Underwater wireless optical communication system channel modelling with oceanic bubbles and water constituents under different wind conditions," *IEEE Photon. J.*, vol. 15, no. 2, pp. 1–11, Apr. 2023, doi: [10.1109/JPHOT.2023.3258500](#).
- [29] S. Q. Duntley, R. W. Austin, W. H. Wilson, C. F. Edgerton, and S. E. Moran, "Ocean color analysis," 1974. [Online]. Available: <https://api.semanticscholar.org/CorpusID:128022252>
- [30] C. D. Mobley, "Estimation of the remote-sensing reflectance from above-surface measurements," *Appl. Opt.*, vol. 38, no. 36, p. 7442, Dec. 1999, doi: [10.1364/AO.38.007442](#).
- [31] P. J. Dev and P. Shanmugam, "Corrigendum to 'A new theory and its application to remove the effect of surface-reflected light in above-surface radiance data from clear and turbid waters' [J. Quant. Spectrosc. Radiat. Transfer 142 (2014) 75–92]," *J. Quantum Spectrosc. Radiat. Transf.*, vol. 147, pp. 288–289, Nov. 2014, doi: [10.1016/j.jqsrt.2014.06.008](#).
- [32] P. Shanmugam, X. He, R. K. Singh, and T. Varunan, "A modern robust approach to remotely estimate chlorophyll in coastal and inland zones," *Adv. Space Res.*, vol. 61, no. 10, pp. 2491–2509, 2018, doi: [10.1016/j.asr.2018.02.024](#).
- [33] S. W. Jeffrey and G. F. Humphrey, "New spectrophotometric equations for determining chlorophylls A, B, C1 and C2 in higher plants, algae and natural phytoplankton," *Biochimie Physiologie der Pflanzen*, vol. 167, no. 2, pp. 191–194, 1975, doi: [10.1016/S0015-3796\(17\)30778-3](#).
- [34] Y. H. Ahn and P. Shanmugam, "Derivation and analysis of the fluorescence algorithms to estimate phytoplankton pigment concentrations in optically complex coastal waters," *J. Opt. A, Pure Appl. Opt.*, vol. 9, no. 4, pp. 352–362, 2007, doi: [10.1088/1464-4258/9/4/008](#).
- [35] E. A. Gokul, P. Shanmugam, B. Sundarabalan, A. Sahay, and P. Chauhan, "Modelling the inherent optical properties and estimating the constituents' concentrations in turbid and eutrophic waters," *Cont. Shelf Res.*, vol. 84, pp. 120–138, Jul. 2014, doi: [10.1016/j.csr.2014.05.013](#).
- [36] R. M. Pope and E. S. Fry, "Absorption spectrum (380–700 nm) of pure water II Integrating cavity measurements," *Appl. Opt.*, vol. 36, no. 33, p. 8710, Nov. 1997, doi: [10.1364/AO.36.008710](#).
- [37] S. S. Prabhakaran, S. K. Sahu, P. J. Dev, and P. Shanmugam, "Modelling the light absorption coefficients of oceanic waters: Implications for underwater optical applications," *J. Mar. Syst.*, vol. 181, pp. 14–24, Jun. 2017, doi: [10.1016/j.jmarsys.2018.02.006](#).
- [38] A. Bricaud, M. Babin, A. Morel, and H. Claustre, "Variability in the chlorophyll-specific absorption coefficients of natural phytoplankton: Analysis and parameterization phytoplankton A o h (A) was analyzed using a data set including 815 spectra determined chlorophyll concentration range Ph values wer," *J. Geophys. Res.*, vol. 100, no. C7, pp. 13321–13332, 1995.
- [39] A. Bricaud, A. Morel, M. Babin, K. Allali, and H. Claustre, "Variations of light absorption by suspended particles with chlorophyll a concentration in oceanic (case 1) waters: Analysis and implications for bio-optical models Abstract. Spectral absorption coefficients of total particulate matter Mg M-3). As pre," *J. Geophys. Res.*, vol. 103, no. C13, pp. 31033–31044, 1998.
- [40] M. Babin, "Variations in the light absorption coefficients of phytoplankton, nonalgal particles, and dissolved organic matter in coastal waters around Europe," *J. Geophys. Res. C, Ocean.*, vol. 108, no. 7, pp. 1–4, 2003, doi: [10.1029/2001jc000882](#).
- [41] P. Shanmugam, "A new bio-optical algorithm for the remote sensing of algal blooms in complex ocean waters," *J. Geophys. Res. Ocean.*, vol. 116, no. 4, pp. 1–12, 2011, doi: [10.1029/2010JC006796](#).
- [42] P. Shanmugam, "New models for retrieving and partitioning the colored dissolved organic matter in the global ocean: Implications for remote sensing," *Remote Sens. Environ.*, vol. 115, no. 6, pp. 1501–1521, 2011, doi: [10.1016/j.rse.2011.02.009](#).
- [43] P. Shanmugam, T. Varunan, S. N. N. Jaiganesh, A. Sahay, and P. Chauhan, "Optical assessment of colored dissolved organic matter and its related parameters in dynamic coastal water systems," *Estuarine, Coastal Shelf Sci.*, vol. 175, pp. 126–145, Jun. 2016, doi: [10.1016/j.ecss.2016.03.020](#).
- [44] R. C. Smith and K. S. Baker, "Optical properties of the clearest natural waters (200–800 nm)," *Appl. Opt.*, vol. 20, no. 2, p. 177, Jan. 1981, doi: [10.1364/AO.20.000177](#).
- [45] X. Zhang and L. Hu, "Estimating scattering of pure water from density fluctuation of the refractive index," *Opt. Exp.*, vol. 17, no. 3, p. 1671, 2009, doi: [10.1364/oe.17.001671](#).
- [46] X. Zhang, L. Hu, and M.-X. He, "Scattering by pure seawater: Effect of salinity," *Opt. Exp.*, vol. 17, no. 7, p. 5698, Mar. 2009, doi: [10.1364/OE.17.005698](#).
- [47] X. Zhang and L. Hu, "Anomalous light scattering by pure seawater," *Appl. Sci.*, vol. 8, no. 12, pp. 1–6, 2018, doi: [10.3390/app8122679](#).
- [48] X. Zhang, D. Stramski, R. A. Reynolds, and E. R. Blocker, "Light scattering by pure water and seawater: The depolarization ratio and its variation with salinity," *Appl. Opt.*, vol. 58, no. 4, p. 991, 2019, doi: [10.1364/ao.58.000991](#).
- [49] L. Hu, X. Zhang, and M. J. Perry, "Light scattering by pure seawater: Effect of pressure," *Deep-Sea Res. I, Oceanographic Res. Papers*, vol. 146, pp. 103–109, Mar. 2019, doi: [10.1016/j.dsr.2019.03.009](#).
- [50] A. Morel and S. Maritorena, "Bio-optical properties of oceanic waters: A reappraisal," *J. Geophys. Res. Ocean.*, vol. 106, no. C4, pp. 7163–7180, 2001, doi: [10.1029/2000jc000319](#).
- [51] C. D. Mobley, "Comparison of numerical models for computing underwater light fields," *Appl. Opt.*, vol. 32, no. 36, p. 7484, Dec. 1993, doi: [10.1364/AO.32.007484](#).
- [52] H. R. Gordon and A. Y. Morel, "In—Water algorithms," in *Remote Assessment of Ocean Color for Interpretation of Satellite Visible Imagery: A Review*. New York, NY, USA: Springer, 1983, pp. 24–67.
- [53] E. A. Gokul and P. Shanmugam, "An optical system for detecting and describing major algal blooms in coastal and oceanic waters around India," *J. Geophys. Res. Ocean.*, vol. 121, no. 6, pp. 4097–4127, Jun. 2016, doi: [10.1002/2015JC011604](#).
- [54] X. Zhang and L. Hu, "Scattering by pure seawater at high salinity," *Opt. Exp.*, vol. 17, no. 15, p. 12685, Jul. 2009, doi: [10.1364/OE.17.012685](#).
- [55] C. D. Mobley and L. K. Sundman, "Hydrolight 4.2 users guide," Sequoia Sci. Inc., Redmond, WA, USA, 2001, p. 87.
- [56] C. D. Mobley and L. K. Sundman, *HydroLight 5.2 User's Guide*. Bellevue, WA, USA: Sequoia Scientific, 2013.
- [57] C. Cox and W. Munk, "Measurement of the roughness of the sea surface from photographs of the Sun's glitter," *J. Opt. Soc. Amer. A, Opt. Image Sci.*, vol. 44, no. 11, p. 838, 1954, doi: [10.1364/josa.44.000838](#).
- [58] P. K. Acharya, "MODTRAN4: Multiple scattering and bidirectional reflectance distribution function (BRDF) upgrades to MODTRAN," *Opt. Spectrosc. Tech. Instrum. Atmos. Space Res. III*, vol. 3756, p. 354, 1999, doi: [10.1117/12.366389](#).
- [59] T. J. Petzold, "Volume scattering functions for selected ocean waters," 1972. [Online]. Available: <https://escholarship.org/uc/item/73p3r43q>
- [60] J. E. O'Reilly, "Ocean color chlorophyll algorithms for SeaWiFS," *J. Geophys. Res. Ocean.*, vol. 103, no. C11, pp. 24937–24953, 1998, doi: [10.1029/98JC02160](#).
- [61] H. J. Nasih, P. Shanmugam, and R. Sundaravadevelu, "Estimation of sediment settling velocity in estuarine and coastal waters using optical remote sensing data," *Adv. Space Res.*, vol. 63, no. 11, pp. 3473–3488, 2019, doi: [10.1016/j.asr.2019.02.023](#).
- [62] Q. Vanhellemont, "Daily metre-scale mapping of water turbidity using CubeSat imagery," *Opt. Exp.*, vol. 27, no. 20, p. A1372, 2019, doi: [10.1364/oe.27.0a1372](#).

- [63] B. Sundarabalan, P. Shanmugam, and S. Manjusha, "Radiative transfer modeling of upwelling light field in coastal waters," *J. Quantum Spectrosc. Radiat. Transf.*, vol. 121, pp. 30–44, 2013, doi: [10.1016/j.jqsrt.2013.01.016](https://doi.org/10.1016/j.jqsrt.2013.01.016).
- [64] B. Sundarabalan and P. Shanmugam, "Modelling of underwater light fields in turbid and eutrophic waters: Application and validation with experimental data," *Ocean Sci.*, vol. 11, no. 1, pp. 33–52, 2015, doi: [10.5194/os-11-33-2015](https://doi.org/10.5194/os-11-33-2015).
- [65] B. Sundarabalan, P. Shanmugam, and Y. H. Ahn, "Modeling the underwater light field fluctuations in coastal oceanic waters: Validation with experimental data," *Ocean Sci. J.*, vol. 51, no. 1, pp. 67–86, 2016, doi: [10.1007/s12601-016-0007-y](https://doi.org/10.1007/s12601-016-0007-y).



**SUNDARABALAN V. BALASUBRAMANIAN** received the Ph.D. degree in ocean optics and satellite remote sensing from the Department of Ocean Engineering, IIT Madras, Chennai, in 2015.

Currently, he is a Research Scientist with Goddard Earth Sciences Technology and Research II (GESTAR-II), University of Maryland at Baltimore County, Baltimore, MD, USA. His research interests include ocean color remote sensing, calibration/validation of ocean satellite

sensors, satellite image processing, atmospheric correction techniques, ocean radiative transfer model, marine optics, ship-borne field measurements, and bio-optical modeling.



**CHAVAPATI GOUSE SANDHANI** received the B.Tech. degree in civil engineering from AP IIIT Nuzvid, RGUKT University, Nuzvid, Andhra Pradesh, India, in 2015, and the M.Tech. degree in environmental engineering and management from IST, JNTUK University, Kakinada, Andhra Pradesh, India, in 2018.

He has been a Ph.D. Scholar with the Department of Ocean Engineering, IIT Madras, Chennai, India. His research interests include effect of bubble

clouds on the remote sensing reflectance and deriving the water color products with and without bubble clouds.



**PALANISAMY SHANMUGAM** received the Ph.D. degree in optical/microwave remote sensing techniques from Anna University, Chennai, India, in 2002.

He is currently a Professor/National Geospatial Chair Professor with the Department of Ocean Engineering, IIT Madras, Chennai. His research interests include ocean optics and imaging, satellite oceanography, radiative transfer in the ocean, algorithm/model development, and underwater

wireless optical communication. He has been a Principal Investigator of several projects funded by the Government of India.



**S. A. SANNASIRAJ** (Senior Member, IEEE) received the Ph.D. degree from the Department of Ocean Engineering, IIT Madras, Chennai, India, in 1997.

He is currently the Chair Professor with the Department of Ocean Engineering, IIT Madras. His area of specialization include climate change impacts on coastal infrastructures, harbors and breakwaters, breaking waves, and wind-wave modeling. He has been a Principal Investigator of

several projects funded by the Government of India. He is the Lead Indian Coordinator of DAAD sponsored Global Water and Climate Adaptation Centre, ABCD.

Dr. Sannasiraj is the Vice-Chair of Executive Council of Asia-Pacific Division of IAHR.

...